

## 1 Mapping single-cell atlases throughout Metazoa unravels cell type evolution

2

3 Alexander J. Tarashansky<sup>1</sup>, Jacob M. Musser<sup>2,§</sup>, Margarita Khariton<sup>1,§</sup>, Pengyang Li<sup>1</sup>,  
4 Detlev Arendt<sup>2,3</sup>, Stephen R. Quake<sup>1,4,5</sup>, Bo Wang<sup>1,6\*</sup>

5

6 <sup>1</sup>Department of Bioengineering, Stanford University, Stanford, CA, USA.

7 <sup>2</sup>European Molecular Biology Laboratory, Developmental Biology Unit, Heidelberg,  
8 Germany.

9 <sup>3</sup>Centre for Organismal Studies, University of Heidelberg, Heidelberg, Germany.

10 <sup>4</sup>Department of Applied Physics, Stanford University, Stanford, CA, USA.

11 <sup>5</sup>Chan Zuckerberg Biohub, San Francisco, CA, USA.

12 <sup>6</sup>Department of Developmental Biology, Stanford University School of Medicine, Stanford,  
13 CA, USA.

14

15 §These authors contributed equally to this work.

16

17 \*Correspondence: [wangbo@stanford.edu](mailto:wangbo@stanford.edu).

18 **Abstract**

19 Comparing single-cell transcriptomic atlases from diverse organisms can elucidate the  
20 origins of cellular diversity and assist the annotation of new cell atlases. Yet,  
21 comparison between distant relatives is hindered by complex gene histories and  
22 diversifications in expression programs. Previously, we introduced the self-assembling  
23 manifold (SAM) algorithm to robustly reconstruct manifolds from single-cell data  
24 (Tarashansky et al., 2019). Here, we build on SAM to map cell atlas manifolds across  
25 species. This new method, SAMap, identifies homologous cell types with shared  
26 expression programs across distant species within phyla, even in complex examples  
27 where homologous tissues emerge from distinct germ layers. SAMap also finds many  
28 genes with more similar expression to their paralogs than their orthologs, suggesting  
29 paralog substitution may be more common in evolution than previously appreciated.  
30 Lastly, comparing species across animal phyla, spanning mouse to sponge, reveals  
31 ancient contractile and stem cell families, which may have arisen early in animal  
32 evolution.

33 **Introduction**

34 There is much ongoing success in producing single-cell transcriptomic atlases to  
35 investigate the cell type diversity within individual organisms (Regev et al., 2017). With  
36 the growing diversity of cell atlases across the tree of life (Briggs et al., 2018; Cao et al.,  
37 2019; Fincher et al., 2018; Hu et al., 2020; Musser et al., 2019; Plass et al., 2018; Siebert  
38 et al., 2019; Wagner et al., 2018), a new frontier is emerging: the use of cross-species  
39 cell type comparisons to unravel the origins of cellular diversity and uncover species-  
40 specific cellular innovations (Arendt et al., 2019; Shafer, 2019). Further, these  
41 comparisons promise to accelerate cell type annotation and discovery by transferring  
42 knowledge from well-studied model organisms to under-characterized animals.

43

44 However, recent comparative single-cell analyses are mostly limited to species within the  
45 same phylum (Baron et al., 2016; Geirsdottir et al., 2019; Sebé-Pedrós et al., 2018;  
46 Tosches et al., 2018). Comparisons across longer evolutionary distances and across  
47 phyla are challenging for two major reasons. First, gene regulatory programs diversify  
48 during evolution, diminishing the similarities in cell type specific gene expression patterns.  
49 Second, complex gene evolutionary history causes distantly related organisms to share  
50 few one-to-one gene orthologs (Nehrt et al., 2011), which are often relied upon for  
51 comparative studies (Briggs et al., 2018; Shafer, 2019). This effect is compounded by the  
52 growing evidence suggesting that paralogs may be more functionally similar than  
53 orthologs across species, due to differential gain (neo-functionalization), loss (non-  
54 functionalization), or partitioning (sub-functionalization) events among paralogs (Nehrt et  
55 al., 2011; Prince & Pickett, 2002; Stamboulian et al., 2020; Studer & Robinson-Rechavi,  
56 2009).

57

58 Here, we present the Self-Assembling Manifold mapping (SAMap) algorithm to enable  
59 mapping single-cell transcriptomes between phylogenetically remote species. SAMap  
60 relaxes the constraints imposed by sequence orthology, using expression similarity  
61 between mapped cells to infer the relative contributions of homologous genes, which in  
62 turn refines the cell type mapping. In addition, SAMap uses a graph-based data  
63 integration technique to identify reciprocally connected cell types across species with  
64 greater robustness than previous single-cell data integration methods (Haghverdi et al.,  
65 2018; Hie et al., 2019; Polański et al., 2019; Stuart et al., 2019).

66

67 Using SAMap, we compared seven whole-body cell atlases from species spanning animal  
68 phylogeny, which have divergent transcriptomes and complex molecular homologies  
69 (**Figure 1A-B** and **Supplementary Table 1**). We began with well-characterized cell types  
70 in developing frog and fish embryos. We found broad concordance between  
71 transcriptomic signatures and ontogenetic relationships, which validated our mapping  
72 results, yet also detected striking examples of homologous cell types emerging from  
73 different germ layers. We next extended the comparison to animals from the same phylum  
74 but with highly divergent body plans, using a planarian flatworm and a parasitic blood  
75 fluke, and found one-to-one homologies even between cell subtypes. Comparing all  
76 seven species from sponge to mouse, we identified densely interconnected cell type  
77 families broadly shared across animals, including contractile and stem cells, along with  
78 their respective gene expression programs. Lastly, we noticed that homologous cell types  
79 often exhibit differential expression of orthologs and similar expression of paralogs,

80 suggesting that the substitution and swapping of paralogs in cell types may be more  
81 common in evolution than previously appreciated. Overall, our study represents an  
82 important step towards analyzing the evolutionary origins of specialized cell types and  
83 their associated gene expression programs in animals.

84 **Results**

85 ***The SAMap algorithm***

86 SAMap iterates between two modules. The first module constructs a gene-gene bipartite  
87 graph with cross-species edges connecting homologous gene pairs, initially weighted by  
88 protein sequence similarity (**Figure 1C**). In the second module, SAMap uses the gene-  
89 gene graph to project the two single-cell transcriptomic datasets into a joint, lower-  
90 dimensional manifold representation, from which each cell's mutual cross-species  
91 neighbors are linked to stitch the cell atlases together (**Figure 1D**). Then, using the joint  
92 manifold, the expression correlations between homologous genes are computed and  
93 used to reweight the edges in the gene-gene homology graph in order to relax SAMap's  
94 initial dependence on sequence similarity. The new homology graph is used as input to  
95 the subsequent iteration of SAMap, and the algorithm continues until convergence,  
96 defined as when the cross-species mapping does not significantly change between  
97 iterations (**Figure 1E**).

98

99 This algorithm overcomes several challenges inherent to mapping single-cell  
100 transcriptomes between distantly related species. First, complex gene evolutionary  
101 history often results in many-to-many homologies with convoluted functional relationships  
102 (Briggs et al., 2018; Nehrt et al., 2011). SAMap accounts for this by using the full  
103 homology graph to project each dataset into both its own and its partner's respective  
104 principal component (PC) spaces, constructed by the SAM algorithm, which we previously  
105 developed to robustly and sensitively identify cell types (Tarashansky et al., 2019). The  
106 resulting within- and cross-species projections are concatenated to form the joint space.

107 For the cross-species projections, we translate each species' features into those of its  
108 partner, with the expression for individual genes imputed as the weighted average of their  
109 homologs specified in the gene-gene bipartite graph. Iteratively refining the homology  
110 graph to only include positively correlated gene pairs prunes the many-to-many  
111 homologies to only include genes that are expressed in the same mapped cell types.

112

113 Second, frequent gene losses and the acquisitions of new genes result in many cell type  
114 gene expression signatures being species-specific, limiting the amount of information that  
115 is comparable across species. Restricting the analysis of each dataset to only include  
116 genes that are shared across species would result in a decreased ability to resolve cell  
117 types and subtypes with many species-specific gene signatures. SAMap solves this  
118 problem by constructing the joint space through the concatenation of within- and cross-  
119 species projections, thus encoding all genes from both species.

120

121 Lastly, the evolution of expression programs gradually diminishes the similarity between  
122 homologous cell types. To account for this effect, SAMap links cell types across species  
123 while tolerating their differences. Cells are mapped by calculating each of their  $k$  mutual  
124 nearest cross-species neighbors in the combined projection. To establish more robust  
125 mutual connectivity, we integrate information from each cell's local, within-species  
126 neighborhood (**Figure 1D**), overcoming the inherent stochasticity of cross-species  
127 correlations. Two cells are thus defined as mutual nearest cross-species neighbors when  
128 their respective neighborhoods have mutual connectivity. It is important to note that the  
129 magnitude of connections is not directly calculated from their expression similarity,

130 allowing cell types with diverged expression profiles to be tightly linked if they are among  
131 each other's closest cross-species neighbors.

132

133 ***Paralog substitutions are prevalent between homologous cell types in frog and fish***

134 We first applied SAMap to the *Xenopus* and zebrafish atlases, which both encompass  
135 embryogenesis until early organogenesis (Briggs et al., 2018; Wagner et al., 2018).  
136 Previous analysis had linked cell types between these two organisms by matching  
137 ontogeny, thereby providing a reference for comparison. SAMap produced a combined  
138 manifold with a high degree of cross-species alignment while maintaining high resolution  
139 for distinguishing cell types in each species (**Figure 2A**). We measured the mapping  
140 strength between cell types by calculating an alignment score (edge width in **Figure 2B**  
141 and color map in **Figure 2C**), defined as the average number of mutual nearest cross-  
142 species neighbors of each cell relative to the maximum possible number of neighbors.

143

144 SAMap revealed broad agreement between transcriptomic similarity and developmental  
145 ontogeny, linking 26 out of 27 expected pairs based on previous annotations (**Figure 2B**  
146 and **Supplementary Table 2**) (Briggs et al., 2018). The only exception is the embryonic  
147 kidney (pronephric duct/mesenchyme), potentially indicating that their gene expression  
148 programs have significantly diverged. In addition, SAMap succeeded in drawing parallels  
149 between the development of homologous cell types and matched time points along  
150 several cell lineages (**Figure 2C**). While the concordance was consistent across cell  
151 types, we noticed that the exact progression of developmental timing can vary, suggesting  
152 that SAMap can quantify heterochrony with cell type resolution.

153

154 SAMap also weakly linked several closely related cell types with different ontogeny. For  
155 example, optic cells from both species are also connected to eye primordium, frog skeletal  
156 muscles to fish presomitic mesoderm, and frog hindbrain to fish forebrain/midbrain.  
157 Notable exceptions also included mapped secretory cell types that differ in their  
158 developmental origin and even arise from different germ layers (black edges in **Figure**  
159 **2B**). They are linked through a large set of genes including conserved transcription factors  
160 (e.g., *foxa1* (Dubaissi et al., 2014), *grhl* (Miles et al., 2017)) and proteins involved in  
161 vesicular protein trafficking (**Figure 2 – figure supplement 1**). This observation supports  
162 the notion that cell types may be transcriptionally and evolutionarily related despite having  
163 different developmental origins (Arendt et al., 2016).

164

165 To benchmark SAMap performance, we used Eggnog (Huerta-Cepas et al., 2019) to  
166 define one-to-one vertebrate orthologs between fish and frog and fed these gene pairs  
167 as input to several broadly used single-cell data integration methods, Seurat (Stuart et  
168 al., 2019), Liger (Welch et al., 2019), Harmony (Korsunsky et al., 2019), Scanorama (Hie  
169 et al., 2019), and BBKNN (Polański et al., 2019). We found that they failed to map the two  
170 atlases, yielding minimal alignment between them (**Figure 2D** and **Figure 2 – figure**  
171 **supplement 2**). We also compared the results when restricting SAMap to using the one-  
172 to-one orthologs instead of the full homology graph. Even when removing the many-to-  
173 many gene homologies and the iterative refinement of the homology graph, we identified  
174 similar, albeit weaker, cell type mappings. This suggests that, at least for the frog and fish

175 comparison, SAMap's performance is owed in large part to its robust, atlas stitching  
176 approach.

177  
178 The key benefit of using the full homology graph is to enable the systematic identification  
179 of gene paralogs that exhibit greater similarity in expression across species than their  
180 corresponding orthologs. These events are expected to arise as the result of gene  
181 duplications followed by diversification of the resulting in-paralogs (Studer & Robinson-  
182 Rechavi, 2009). In addition, genetic compensation by transcriptional adaptation, where  
183 loss-of-function mutations are balanced by upregulation of related genes with similar  
184 sequences (El-Brolosy et al., 2019), could also result in this signature. In total, SAMap  
185 selected 8,286 vertebrate orthologs and 7,093 eukaryotic paralogs, as enumerated by  
186 Eggnog, for manifold alignment. Among these, 565 genes have markedly higher  
187 expression correlations (correlation difference  $> 0.3$ ) with their paralogs than their  
188 orthologs (**Figure 2E** and **Figure 2 – figure supplement 3**), and 209 genes have  
189 orthologs that are either completely absent or lowly-expressed with no cell-type specificity  
190 (**Supplementary Table 3**), suggesting that they may have lost their functional roles at  
191 some point and were compensated for by their paralogs. We term these events as  
192 “paralog substitutions”. SAMap linked an additional 297 homologous pairs not previously  
193 annotated by orthology or paralogy, but which exhibited sequence similarity and high  
194 expression correlations ( $>0.5$  Pearson correlation). These likely represent unannotated  
195 orthologs/paralogs or isofunctional, distantly related homologs (Gabaldón & Koonin,  
196 2013). These results illustrate the potential of SAMap in leveraging single-cell gene  
197 expression data for pruning the networks of homologous genes to identify evolutionary

198 substitution of paralogs and, more generally, identify non-orthologous gene pairs that may  
199 perform similar functions in the cell types within which they are expressed.

200

201 ***Homologous cell types between two flatworm species with divergent body plans***

202 To test if we can identify homologous cell types in animals with radically different body  
203 plans, we mapped the cell atlases of two flatworms, the planarian *Schmidtea*  
204 *mediterranea* (Fincher et al., 2018), and the trematode *Schistosoma mansoni*, which we  
205 collected recently (Li et al., 2020). They represent two distant lineages within the same  
206 phylum but have remarkably distinct body plans and autecology (Laumer et al., 2015;  
207 Littlewood & Waeschenbach, 2015). While planarians live in freshwater and are known  
208 for their ability to regenerate (Reddien, 2018), schistosomes live as parasites in humans.  
209 The degree to which cell types are conserved between them is unresolved, given the vast  
210 phenotypic differences caused by the transition from free-living to parasitic habits  
211 (Laumer et al., 2015).

212

213 SAMap revealed broad cell type homology between schistosomes and planarians. The  
214 schistosome had cells mapped to the planarian stem cells, called neoblasts, as well as  
215 most of the differentiated tissues: neural, muscle, intestine, epidermis, parenchymal,  
216 protonephridia, and *cathepsin*<sup>+</sup> cells, the latter of which consists of cryptic cell types that,  
217 until now, have only been found in planarians (Fincher et al., 2018) (**Figure 3A**). These  
218 mappings are supported by both known cell type specific marker genes and numerous  
219 homologous transcriptional regulators (**Figure 3B** and **Figure 3 – figure supplement 1**).

220

221 We next determined if cell type homologies exist at the subtype level. For this, we  
222 compared the neoblasts, as planarian neoblasts are known to comprise populations of  
223 pluripotent cells and tissue-specific progenitors (Fincher et al., 2018; Zeng et al., 2018).  
224 By mapping the schistosome neoblasts to a planarian neoblast atlas (Zeng et al., 2018),  
225 we found that the schistosome has a population of neoblasts ( $\epsilon$ -cells (Wang et al., 2018))  
226 that cluster with the planarian's pluripotent neoblasts, both expressing a common set of  
227 TFs (e.g., *soxp2*, *unc4*, *pax6a*, *gcm1*) (**Figure 3C-D**). The  $\epsilon$ -cells are closely associated  
228 with juvenile development and lost in adult schistosomes (Wang et al., 2018), indicating  
229 pluripotent stem cells may be a transient population restricted to their early developmental  
230 stages. This is consistent with the fact that, whereas schistosomes can heal wounds, they  
231 have limited regenerative ability (Wendt & Collins, 2016). SAMap also linked other  
232 schistosome neoblast populations with planarian progenitors, including two populations  
233 of schistosome neoblasts (denoted as  $\mu$  (Tarashansky et al., 2019) and  $\mu'$ ) to planarian  
234 muscle progenitors, all of which express *myoD*, a canonical master regulator of  
235 myogenesis (Scimone et al., 2017). These likely represent early and late muscle  
236 progenitors, respectively, as  $\mu$ -cells do not yet express differentiated muscle markers  
237 such as *troponin*, whereas  $\mu'$ -cells do (**Figure 3 – figure supplement 2**).  
238

### 239 ***Cell type families spanning the animal tree of life***

240 To compare cell types across broader taxonomic scales, we extended our analysis to  
241 include juvenile freshwater sponge (*Spongilla lacustris*) (Musser et al., 2019), adult *Hydra*  
242 (*Hydra vulgaris*) (Siebert et al., 2019), and mouse (*Mus musculus*) embryogenesis  
243 (Pijuan-Sala et al., 2019) atlases. In total, SAMap linked 1,051 cross-species pairs of cell

244 types, defined by the annotations used in each respective study. 95% of the cell type  
245 pairs are supported by at least 40 enriched gene pairs, and 87% are supported by more  
246 than 100 gene pairs, indicating that SAMap does not spuriously connect cell types with  
247 limited overlap in expression profiles (**Figure 4A**).

248  
249 We next extended the notion of cell type pairs to cell type trios, as mapped cell types gain  
250 additional support if they share transitive relationships to other cell types through  
251 independent mappings, forming cell type triangles among species. The transitivity of a  
252 cell type pair (edge) or a cell type (node) can be quantified as the fraction of triads to  
253 which they belong that form triangles (**Figure 4B**). The majority (81%) of cell type pairs  
254 have non-zero transitivity independent of alignment score and the number of enriched  
255 gene pairs (**Figure 4 – figure supplement 1-2**). Cell type pairs with fewer than 40  
256 enriched gene pairs tend to have lower (<0.4) transitivity (**Figure 4 – figure supplement**  
257 **2**). In addition, 16% of mapped cell type pairs have zero edge transitivity but non-zero  
258 node transitivity, meaning that at least one of the cell types connects to only a single  
259 member of an interconnected cell type group (**Figure 4C**). Such edges may be of lower  
260 confidence as they should connect to other members of the same group and are thus  
261 excluded from downstream analysis.

262  
263 Among the interconnected groups of cell types, we identified families of contractile cells  
264 and neural cells (**Figure 4D**). Both cell type families are highly transitive compared to the  
265 overall graph transitivity (bootstrap p-value  $< 1 \times 10^{-5}$ ), meaning that their constituent cell  
266 types have more transitive edges within the group than outside the group (**Figure 4E**). In

267 addition, the dense, many-to-many connections within the contractile and neural families  
268 are each supported by at least 40 enriched gene pairs (**Figure 4F**). Consistent with the  
269 nerve net hypothesis suggesting a unified origin of neural cell types (Tosches & Arendt,  
270 2013), the neural family includes vertebrate brain tissues, both bilaterian and cnidarian  
271 neurons, cnidarian nematocytes that share the excitatory characteristics of neurons (Weir  
272 et al., 2020), and *Spongilla* choanocytes and apopylar cells, both of which are not  
273 considered as neurons but have been shown to express postsynaptic-like scaffolding  
274 machinery (Musser et al., 2019; Wong et al., 2019). The contractile family includes  
275 myocytes in bilaterian animals, *Hydra* myoepithelial cells that are known to have  
276 contractile myofibrils (Buzgariu et al., 2015), and sponge pinacocytes and  
277 myopeptidocytes, both of which have been implicated to play roles in contractility (Musser  
278 et al., 2019; Sebé-Pedrós et al., 2018). In contrast to the families encompassing all seven  
279 species, we also found a fully interconnected group that contains invertebrate pluripotent  
280 stem cells, including planarian and schistosome neoblasts, *Hydra* interstitial cells, and  
281 sponge archeocytes (Alié et al., 2015). The lack of one-to-one connections across phyla  
282 is in keeping with recent hypotheses that ancestral cell types diversified into families of  
283 cell types after speciation events (Arendt et al., 2016, 2019). Our findings thus suggest  
284 that these cell type families diversified early in animal evolution.

285

### 286 ***Transcriptomic signatures of cell type families***

287 The high interconnectedness between cell types across broad taxonomic scales suggests  
288 that they should share ancestral transcriptional programs (Arendt et al., 2016; Tosches  
289 et al., 2018). SAMap identified broad transcriptomic similarity between bilaterian and non-

290 bilaterian contractile cells that extends beyond the core contractile apparatus. It links a  
291 total of 23,601 gene pairs, connecting 5,471 unique genes, which are enriched in at least  
292 one contractile cell type pair. Performing functional enrichment analysis on these genes,  
293 we found cytoskeleton and signal transduction functions to be enriched ( $p$ -value  $< 10^{-3}$ )  
294 based on the KOG functional classifications (Tatusov et al., 2003) assigned by EggNOG  
295 (**Figure 5A**). These genes include orthology groups spanning diverse functional roles in  
296 contractile cells, including actin regulation, cell adhesion and stability, and signaling  
297 (**Figure 5B** and **Supplementary Table 4**), indicating that contractile cells were likely  
298 multifunctional near the beginning of animal evolution.

299

300 We also identified several transcriptional regulators shared among contractile cells  
301 (**Figure 5B**). Previously known core regulators involved in myocyte specification (Brunet  
302 et al., 2016) were enriched only in bilaterian (e.g., *myod*, and *tcf4/E12*) or vertebrate  
303 contractile cells (e.g., *mef2*). In contrast, we found homologs of Muscle Lim Protein (*Csrp*)  
304 and Forkhead Box Group 1 (Larroux et al., 2008) enriched in contractile cells from all  
305 seven species. The Fox proteins included FoxC, which is known to regulate cardiac  
306 muscle identity in vertebrates (Brunet et al., 2016) and is contractile-specific in all species  
307 except schistosome and *Spongilla*. Notably, we also identified FoxG orthologs to be  
308 enriched in three of the four invertebrates (**Figure 5 – figure supplement 1**), suggesting  
309 that FoxG may play an underappreciated role in contractile cell specification outside  
310 vertebrates.

311

312 For the family of invertebrate stem cells, we identified 3,343 genes that are enriched in at  
313 least one cell type pair and observed significant enrichment (p-value < 10<sup>-3</sup>) of genes  
314 involved in translational regulation such as RNA processing, translation, and post-  
315 translational modification (**Figure 5C**). These genes form 979 orthology groups, 17% of  
316 which are enriched in all cell types of this family (**Supplementary Table 4**). Importantly,  
317 other stem cell populations in *Hydra* and planarian lineage-restricted neoblasts have  
318 significantly reduced expression of these genes (**Figure 5D**). These results suggest that  
319 SAMap identified a large, deeply conserved gene module specifically associated with  
320 multipotency.

321

## 322 **Discussion**

323 Cell types evolve as their gene expression programs change either as integrated units or  
324 via evolutionary splitting that results in separate derived programs. While this notion of  
325 coupled cellular and molecular evolution has gained significant traction in the past years,  
326 systematically comparing cell type-specific gene expression programs across species  
327 has remained a challenging problem. Here, we map single-cell atlases between  
328 evolutionarily distant species in a manner that accounts for the complexity of gene  
329 evolution. SAMap aligns cell atlases in two mutually reinforcing directions, mapping both  
330 the genes and the cells, with each feeding back into the other. This method allows us to  
331 identify one-to-one cell type concordance between animals in the same phylum, whereas  
332 between phyla, we observe interconnected cell types forming distinct families. These  
333 findings support the notion that cell types evolve via hierarchical diversification (Arendt et  
334 al., 2019), resulting in cell type families composed of evolutionarily related cell types

335 sharing a regulatory gene expression program that originated in their common ancestor.  
336 One-to-one cell type homologies should exist only if no further cell type diversification has  
337 occurred since the speciation.

338  
339 In parallel, SAMap systematically identifies instances where paralogs exhibit greater  
340 expression similarity than orthologs across species. Paralog substitution likely occurs due  
341 to differential loss or retention of cell type-specific expression patterns of genes that were  
342 duplicated in the common ancestor (Studer & Robinson-Rechavi, 2009). Alternatively,  
343 paralog substitutions could arise due to compensating upregulation of paralogs following  
344 a loss-of-function mutation acquired by an ortholog (El-Brolosy et al., 2019). While the  
345 analysis presented here focuses on comparisons between two species, incorporating  
346 multiple species into a single analysis that also accounts for their phylogenetic  
347 relatedness could enable determining the specific order of paralog substitutions,  
348 associated cell type diversification events, and the mechanism by which they arose.  
349 However, this would require cell atlases that consistently sample key branching points  
350 along the tree of life. Nevertheless, identifying lineage-specific paralog substitution  
351 signatures should be accessible in extensively studied vertebrate single-cell atlases, as  
352 the vertebrate clade is where existing data and knowledge are most concentrated.

353  
354 Besides applications in evolutionary biology, we anticipate SAMap can catalyze the  
355 annotation of new cell atlases from non-model organisms, which often represents a  
356 substantial bottleneck requiring extensive manual curation and prior knowledge. Its ability  
357 to use the existing atlases to inform the annotation of cell types in related species will

358 keep improving as more datasets become available to better sample the diversity of cell  
359 types. Moreover, our approach allows leveraging existing and forthcoming single-cell  
360 gene expression data to predict functionally similar gene homologs, which can serve as  
361 guideposts for mechanistic molecular studies.

362

363 **Materials and Methods**

364 ***Data and Code Availability***

- 365 • The source code for SAMap is publicly available at Github  
366 (<https://github.com/atarashansky/SAMap>), along with the code to perform the  
367 analysis and generate the figures.
- 368 • The datasets analyzed in this study are detailed in **Supplementary Table 1** with  
369 their accessions, and annotations provided.

370

371 ***The SAMap Algorithm***

372

373 The SAMap algorithm contains three major steps: preprocessing, mutual nearest  
374 neighborhood alignment, and gene-gene correlation initialization. The latter two are  
375 repeated for three iterations, by default, to balance alignment performance and  
376 computational runtime. SAMap runs up to one hour on an average desktop computer for  
377 200,000 total cells.

378

379 1. *Preprocessing*.

380 1.1. *Generate gene homology graph via reciprocal BLAST*.

381 We first construct a gene-gene bipartite graph between two species by performing  
382 reciprocal BLAST of their respective transcriptomes using *tblastx*, or proteomes using  
383 *blastp*. *tblastn* and *blastx* are used for BLAST between proteome and transcriptome.  
384 When a pair of genes share multiple High Scoring Pairs (HSPs), which are local regions

385 of matching sequences, we use the HSP with the highest bit score to measure homology.

386 Only pairs with E-value  $< 10^{-6}$  are included in the graph.

387

388 Here we define similarity using BLAST, though SAMap is compatible with other protein  
389 homology detection methods (e.g. HMMER (Eddy, 2008)) or orthology inference tools  
390 (e.g. OrthoClust (Yan et al., 2014) and EggnoG (Huerta-Cepas et al., 2019)). While each  
391 of these methods has known strengths and limitations, BLAST is chosen for its broad  
392 usage, technical convenience, and compatibility with low-quality transcriptomes.

393

394 We encode the BLAST results into two triangular adjacency matrices,  $A$  and  $B$ , each  
395 containing bit scores in one BLAST direction. We combine  $A$  and  $B$  to form a gene-gene  
396 adjacency matrix  $G$ . After symmetrizing  $G$ , we remove edges that only appear in one  
397 direction:  $G = Recip(\frac{1}{2}[(A + B) + (A + B)^T]) \in \mathbb{R}^{m_1+m_2 \times m_1+m_2}$ , where  $Recip$  only keeps  
398 reciprocal edges, and  $m_1$  and  $m_2$  are the number of genes of the two species,  
399 respectively. To filter out relatively weak homologies, we also remove edges where  $G_{ab} <$   
400  $0.25 \max_b(G_{ab})$ . Edge weights are then normalized by the maximum edge weight for each  
401 gene and transformed by a hyperbolic tangent function to increase discriminatory power  
402 between low and high edge weights,  $\hat{G}_{ab} = 0.5 + 0.5 \tanh(10G_{ab}/\max_b(G_{ab}) - 5)$ .

403

404 *1.2. Construct manifolds for each cell atlas separately using the SAM algorithm.*

405 The scRNAseq datasets are normalized such that each cell has a total number of raw  
406 counts equal to the median size of single-cell libraries. Gene expressions are then log-  
407 normalized with the addition of a pseudocount of 1. Genes expressed (i.e.,  $\log_2(D + 1) >$

408 1) in greater than 96% of cells are filtered out. SAM is run using the following parameters:  
409 *preprocessing* = 'StandardScaler', *weight\_PCs* = *False*, *k* = 20, and *npcs* = 150. A detailed  
410 description of parameters is provided previously (Tarashansky et al., 2019). SAM outputs  
411  $N_1$  and  $N_2$ , which are directed adjacency matrices that encode  $k$ -nearest neighbor graphs  
412 for the two datasets, respectively.

413  
414 SAM only includes the top 3,000 genes ranked by SAM weights and the first 150 principal  
415 components (PCs) in the default mode to reduce computational complexity. However,  
416 downstream mapping requires PC loadings for all genes. Thus, in the final iteration of  
417 SAM, we run PCA on all genes and take the top 300 PCs. This step generates a loading  
418 matrix for each species  $i$ ,  $L_i \in \mathbb{R}^{300 \times m_i}$ .

419  
420 2. *Mutual nearest neighborhood alignment*.  
421 2.1. *Transform feature spaces between species*.  
422 For the gene expression matrices  $Z_i \in \mathbb{R}^{n_i \times m_i}$ , where  $n$  and  $m$  are the number of cells  
423 and genes respectively, we first zero the expression of genes that do not have an edge  
424 in  $\hat{G}$  and standardize the expression matrices such that each gene has zero mean and  
425 unit variance, yielding  $\tilde{Z}_i$ .  $\hat{G}$  represents a bipartite graph in the form of  $\hat{G} =$   
426 
$$\begin{bmatrix} 0_{m_1, m_1} & H \in \mathbb{R}^{m_1 \times m_2} \\ H^T \in \mathbb{R}^{m_2 \times m_1} & 0_{m_2, m_2} \end{bmatrix}$$
, where  $0_{m, m}$  is  $m \times m$  zero matrix and  $H$  is the biadjacency  
427 matrix. Letting  $H_1 = H$  and  $H_2 = H^T$  encoding directed edges from species 1 to 2 and 2  
428 to 1, respectively, we normalize the biadjacency matrix  $H_i$  such that each row sums to 1:  
429  $\hat{H}_i = \text{SumNorm}(H_i) \in \mathbb{R}^{m_i \times m_j}$ , where the *SumNorm* function normalizes the rows to sum

430 to 1. The feature spaces can be transformed between the two species via weighted  
431 averaging of gene expression,  $\tilde{Z}_{ij} = \tilde{Z}_i \hat{H}_i$ .

432

433 *2.2. Project single-cell gene expressions into a joint PC space.*

434 We project the expression data from two species into a joint PC space (Barkas et al.,  
435 2019),  $P_i = \tilde{Z}_i L_i^T$  and  $P_{ij} = \tilde{Z}_{ij} L_j^T$ . We then horizontally concatenate the principal  
436 components  $P_i$  and  $P_{ij}$  to form  $\hat{P}_i \in \mathbb{R}^{n_i \times 600}$ .

437

438 *2.3. Calculate k-nearest cross-species neighbors for all cells.*

439 Using the joint PCs,  $\hat{P}_i$ , we identify for each cell the  $k$ -nearest neighbors in the other  
440 dataset using cosine similarity ( $k = 20$  by default). Neighbors are identified using the  
441 *hnswlib* library, a fast approximate nearest-neighbor search algorithm (Malkov &  
442 Yashunin, 2020). This outputs two directed biadjacency matrices  $C_i \in \mathbb{R}^{n_i \times n_j}$  for  $(i, j) =$   
443 (1,2) or (2,1) with edge weights equal to the cosine similarity between the PCs.

444

445 *2.4. Apply the graph-coarsening mapping kernel to identify cross-species mutual nearest  
446 neighborhoods.*

447 To increase the stringency and confidence of mapping, we only rely on cells that are  
448 *mutual* nearest cross-species neighbors, which are typically defined as two cells  
449 reciprocally connected to one another (Haghverdi et al., 2018). However, due to the noise  
450 in cell-cell correlations and stochasticity in the kNN algorithms, cross-species neighbors  
451 are often randomly assigned from a pool of cells that appear equally similar, decreasing  
452 the likelihood of mutual connectivity between individual cells even if they have similar

453 expression profiles. To overcome this limitation, we integrate information from each cell's  
454 local neighborhood to establish more robust mutual connectivity between cells across  
455 species. Two cells are thus defined as mutual nearest cross-species neighbors when their  
456 respective neighborhoods have mutual connectivity.

457

458 Specifically, the nearest neighbor graphs  $N_i$  calculated in step 1.2 are used to calculate  
459 the neighbors of cells  $t_i$  hops away along outgoing edges:  $\bar{N}_i = N_i^{t_i}$ , where  $\bar{N}_i$  are  
460 adjacency matrices that contain the number of paths connecting two cells  $t_i$  hops away,  
461 for  $i = 1$  or  $2$ .  $t_i$  determines the length-scale over which we integrate incoming edges for  
462 species  $i$ . Its default value is 2 if the dataset size is less than 20,000 cells and 3 otherwise.  
463 However, cells within tight clusters may have spurious edges connecting to other parts of  
464 the manifold only a few hops away. To avoid integrating neighborhood information outside  
465 this local structure, we use the Leiden algorithm (Traag et al., 2019) to cluster the graph  
466 and identify a local neighborhood size for each cell (the resolution parameter is set to 3  
467 by default). If cell  $a$  belongs to cluster  $c_a$ , then its neighborhood size is  $l_a = |c_a|$ . For each  
468 row  $a$  in  $\bar{N}_i$  we only keep the  $l_a$  geodesically closest cells, letting the pruned graph be  
469 denoted as  $\hat{N}_i$ .

470

471 Edges outgoing from cell  $a_i$  in species  $i$  are encoded in the corresponding row in the  
472 adjacency matrix:  $C_{i,a_i}$ . We compute the fraction of the outgoing edges from each cell that  
473 target the local neighborhood of a cell in the other species:  $\tilde{C}_{i,a_i b_j} = \sum_{c \in X_{j,b_j}} C_{i,a_i c}$ , where  
474  $X_{j,b_j}$  is the set of cells in the neighborhood of cell  $b_j$  in species  $j$  and  $\tilde{C}_{i,a_i b_j}$  is the fraction

475 of outgoing edges from cell  $a_i$  in species  $i$  targeting the neighborhood of cell  $b_j$  in species  
476  $j$ .

477

478 To reduce the density of  $\tilde{C}_i$  so as to satisfy computational memory constraints, we remove  
479 edges with weight less than 0.1. Finally, we apply the mutual nearest neighborhood  
480 criterion by taking the element-wise, geometric mean of the two directed bipartite graphs:  
481  $\tilde{C} = \sqrt{\tilde{C}_1 \circ \tilde{C}_2}$ . This operation ensures that only bidirectional edges are preserved, as small  
482 edge weights in either direction results in small geometric means.

483

484 *2.5. Assign the  $k$ -nearest cross-species neighborhoods for each cell and update edge  
485 weights in the gene homology graph.*

486 Given the mutual nearest neighborhoods  $\tilde{C} \in \mathbb{R}^{n_1 \times n_2}$ , we select the  $k$  nearest  
487 neighborhoods for each cell in both directions to update the directed biadjacency matrices  
488  $C_1$  and  $C_2$ :  $C_1 = KNN(\tilde{C}, k)$  and  $C_2 = KNN(\tilde{C}^T, k)$ , with  $k = 20$  by default.

489

490 *2.6. Stitch the manifolds.*

491 We use  $C_1$  and  $C_2$  to combine the manifolds  $N_1$  and  $N_2$  into a unified graph. We first weight  
492 the edges in  $N_1$  and  $N_2$  to account for the number of shared cross-species neighbors by  
493 computing the one-mode projections of  $C_1$  and  $C_2$ . In addition, for cells with strong cross-  
494 species alignment, we attenuate the weight of their within-species edges. For cells with  
495 little to no cross-species alignment, their within-species are kept the same to ensure that  
496 the local topological information around cells with no alignment is preserved.

497

498 Specifically, we use  $N_1$  and  $N_2$  to mask the edges in the one-mode projections,  $\tilde{N}_1 =$   
499  $U(N_1) \circ (Norm(C_1)Norm(C_2))$  and  $\tilde{N}_2 = U(N_2) \circ (Norm(C_2)Norm(C_1))$ , where  $U(E)$  sets  
500 all edge weights in graph  $E$  to 1 and  $Norm$  normalizes the outgoing edges from each cell  
501 to sum to 1. The minimum edge weight is set to be 0.3 to ensure that neighbors in the  
502 original manifolds with no shared cross-species neighbors still retain connectivity:  $\tilde{N}_{1,ij} =$   
503  $\min(0.3, \tilde{N}_{1,ij})$  and  $\tilde{N}_{2,ij} = \min(0.3, \tilde{N}_{2,ij})$  for all edges  $(i,j)$ . We then scale the within-  
504 species edges from cell  $i$  by the total weight of its cross-species edges:  $\tilde{N}_{1,i} = (1 -$   
505  $\frac{1}{k} \sum_{j=1}^{n_2} C_{1,ij}) \tilde{N}_{1,i}$  and  $\tilde{N}_{2,i} = (1 - \frac{1}{k} \sum_{j=1}^{n_1} C_{2,ij}) \tilde{N}_{2,i}$ . Finally, the within- and cross-species  
506 graphs are stitched together to form the combined nearest neighbor graph  $N$ :  $N = [\tilde{N}_1 \oplus$   
507  $C_1] \oplus [C_2 \oplus \tilde{N}_2]$ . The overall alignment score between species 1 and 2 is defined as  $S =$   
508  $\frac{1}{n_1+n_2} (\sum_{i=1}^{n_1} \sum_{j=1}^{n_2} C_{1,ij} + \sum_{i=1}^{n_2} \sum_{j=1}^{n_1} C_{2,ij})$ .

509

510 3. *Gene-gene correlation initialization.*

511 3.1. *Update edge weights in the gene-gene bipartite graph with expression correlations.*

512 To compute correlations between gene pairs, we first transfer expressions from one  
513 species to the other:  $\bar{Z}_{i,n_i m_j} = C_{i,n_i} Z_{j,m_j}$ , where  $\bar{Z}_{i,n_i m_j}$  is the imputed expressions of gene  
514  $m_j$  from species  $j$  for cell  $n_i$  in species  $i$ , and  $C_{i,n_i}$  is row  $n_i$  of the biadjacency matrix  
515 encoding the cross-species neighbors of cell  $n_i$  in species  $i$ , all for  $(i,j) = (1,2)$  and  $(2,1)$ .  
516 We similarly use the manifolds constructed by SAM to smooth the within-species gene  
517 expressions using kNN averaging:  $\bar{Z}_{j,m_j} = N_j Z_{j,m_j}$ , where  $N_j$  is the nearest-neighbor  
518 graph for species  $j$ . We then concatenate the within- and cross-species gene expressions  
519 such that the expression of gene  $m_j$  from species  $j$  in both species is  $\bar{Z}_{m_j} = \bar{Z}_{i,m_j} \oplus \bar{Z}_{j,m_j}$ .

520

521 For all gene pairs in the unpruned homology graph generated in step 1.1.,  $\hat{G}$ , we compute  
522 their correlations,  $\hat{G}_{ab} := \theta(0) \text{Corr}(\bar{Z}_a, \bar{Z}_b)$ , where  $\theta(0)$  is a Heaviside step function  
523 centered at 0 to set negative correlations to zero. We then use the expression correlations  
524 to update the corresponding edge weights in  $\hat{G}$ , which are again normalized through  
525  $\hat{G}_{ab} = 0.5 + 0.5 \tanh(10\hat{G}_{ab}/\max_b(\hat{G}_{ab}) - 5)$ .

526

### 527 **Annotation of cell atlases**

528 To annotate the primary zebrafish and *Xenopus* cell types, the cell subtype annotations  
529 provided by the original publications (Briggs et al., 2018; Wagner et al., 2018) are  
530 coarsened using a combination of the manual matching and developmental hierarchies.  
531 For example, as “heart - mature”, “heart - hoxd9a”, “heart”, and “heart field” in zebrafish  
532 are all manually matched to “cardiac mesoderm” in *Xenopus*, we label these cells as  
533 “heart”. In cases where the matching is insufficient to coarsen the annotations, we use  
534 the provided developmental trees to name a group of terminal cell subtypes by their  
535 common ontogenetic ancestor. The annotations provided by their respective studies were  
536 used to label the cells in the *Spongilla*, *Hydra*, and mouse atlases. To annotate the  
537 schistosome cells, we used known marker genes to annotate the main schistosome tissue  
538 types (Li et al., 2020). Annotations for all single cells in all datasets are provided in

539 **Supplementary Table 1.**

540

### 541 **Visualization**

542 The combined manifold  $N$  is embedded into 2D projections using UMAP implemented in

543 the scanpy package (Wolf et al., 2018) by `scanpy.tl.umap` with the parameter `min_dist` =  
544 0.1. The sankeyD3 package (<https://rdrr.io/github/fbreitwieser/sankeyD3/man/sankeyD3-package.html>) in R is used to generate the sankey plots. Edge thickness corresponds to  
545 the alignment score between mapped cell types. The alignment score between cell types  
546 the alignment score between mapped cell types. The alignment score between cell types  
547  $a$  and  $b$  is defined as  $s_{ab} = \frac{1}{|c_a|+|c_b|} (\sum_{i \in c_a} \sum_{j \in c_b} C_{1,ij} + \sum_{i \in c_b} \sum_{j \in c_a} C_{2,ij})$ , where  $c_a$  and  $c_b$   
548 are the set of cells in cell types  $a$  and  $b$ , respectively. Cell type pairs with alignment score  
549 less than  $z$  are filtered out. By default,  $z$  is set to be 0.1. Cell types that did not cluster  
550 properly in their respective manifolds were omitted from the sankey plot. In the zebrafish-  
551 *Xenopus* comparison, we excluded heart, germline, and olfactory placode cells from both  
552 species because they did not cluster in the *Xenopus* atlas. Similarly, the iridoblast,  
553 epiphysis, *nanog*+, apoptotic-like, and forerunner cells were excluded because they did  
554 not cluster in the zebrafish atlas.

555  
556 The network graphs in **Figure 4D** are generated using the `networkx` package  
557 (<https://networkx.github.io>) in python. To focus on densely connected cell type groups,  
558 we filter out cell type pairs with alignment score less than 0.05.

559  
560 ***Identification of gene pairs that drive cell type mappings***  
561 We define  $g_1$  and  $g_2$  to contain SAMap-linked genes from species 1 and 2, respectively.  
562 Note that a gene may appear multiple times as SAMap allows for one-to-many homology.  
563 Let  $X_{a_1 b_2}$  denote the set of all cells with cross species edges between cell types  $a_1$  and  
564  $b_2$ . We calculate the average standardized expression of all cells from species  $i$  that are  
565 in  $X_{a_1 b_2}$ :  $Y_{i,g_i} = \frac{1}{|\{x, x \in X_{a_1 b_2}\}|} \sum_{x \in X_{a_1 b_2}} \tilde{Z}_{i,x,g_i}$ , where  $\tilde{Z}_{i,x,g_i} \in \mathfrak{R}^{|g_i|}$  is the standardized

566 expression of genes  $g_i$  in cell  $x$ . The correlation between  $Y_{1,g_1}$  and  $Y_{2,g_2}$  can be written as  
567  $\text{Corr}(Y_{1,g_1}, Y_{2,g_2}) = \sum_{j=1}^{|g_1|} S(Y_{1,g_1})_j \circ S(Y_{2,g_2})_j$ , where  $S(Z)$  standardizes vector  $Z$  to have  
568 zero mean and unit variance. We use the summand to identify gene pairs that contribute  
569 most positively to the correlation. We assign each gene pair a score:  $h_g = T(S(Y_{1,g_1})) \circ$   
570  $T(S(Y_{2,g_2}))$ , where  $T(Z)$  sets negative values in vector  $Z$  to zero in order to ignore lowly-  
571 expressed genes. To be inclusive, we begin with the top 1,000 gene pairs according to  
572  $h_g$  and filter out gene pairs in which one or both of the genes are not differentially  
573 expressed in their respective cell types ( $p\text{-value} > 10^{-2}$ ), have less than 0.2 SAM weight,  
574 or are expressed in fewer than 5% of the cells in the cluster. The differential expression  
575 of each gene in each cell type is calculated using the Wilcoxon rank-sum test  
576 implemented in the `scanpy` function `scanpy.tl.rank_genes_groups`.

577  
578 **Orthology group assignment**  
579 We used the Eggnog mapper (v5.0) (Huerta-Cepas et al., 2019) to assign each gene to  
580 an orthology group with default parameters. For the zebrafish-to-*Xenopus* mapping,  
581 genes are considered paralogs if they map to the same eukaryotic orthology group and  
582 orthologs if they map to the same vertebrate orthology group. For the pan-species  
583 analysis, we group genes from all species with overlapping orthology assignments. In  
584 **Figure 5B**, each column corresponds to one of these groups. As each group may contain  
585 multiple genes from each species, we present the expression of the gene with the highest  
586 enrichment score per species. All gene names and corresponding orthology groups are  
587 reported in **Supplementary Table 4**.

588

589 ***Phylogenetic reconstruction of gene trees***

590 We generate gene trees to validate the identity of genes involved in putative examples of  
591 paralog substitution and of *Fox* and *Csrp* transcriptional regulators that are identified as  
592 enriched in contractile cells. For this, we first gather protein sequences from potential  
593 homologs using the eggNOG version 5.0 orthology database (Huerta-Cepas et al., 2019).  
594 For the *Fox* and *Csrp* phylogenies, we include all *Fox* clade I (Larroux et al., 2008) and  
595 *Csrp/Crip* homologs, respectively, from the seven species included in our study.

596

597 Alignment of protein sequences is performed with Clustal Omega version 1.2.4 using  
598 default settings as implemented on the EMBL EBI web services platform (Madeira et al.,  
599 2019). Maximum likelihood tree reconstruction is performed using IQ-TREE version  
600 1.6.12 (Nguyen et al., 2015) with the ModelFinder Plus option (Kalyaanamoorthy et al.,  
601 2017). For the *Csrp* tree, we perform 1,000 nonparametric bootstrap replicates to assess  
602 node support. For *Fox*, we utilize the ultrafast bootstrap support option with 1,000  
603 replicates. For each gene tree we choose the model that minimizes the Bayesian  
604 Information Criterion (BIC) score in ModelFinder. This results in selection of the following  
605 models: DCMut+R4 (*Csrp*) and VT+F+R5 (*Fox*). The final consensus trees are visualized  
606 and rendered using the ete3 v3.1.1 python toolkit (Huerta-Cepas et al., 2016) and the  
607 Interactive Tree of Life v4 (Letunic & Bork, 2019).

608

609 ***KOG functional annotation and enrichment analysis***

610 Using the eggNOG mapper, KOG functional annotations are transferred to individual  
611 transcripts from their assigned orthology group. For enrichment analysis, all genes

612 enriched in the set of cell type pairs of interest are lumped to form the target set for each  
613 species. For example, the target set for *Spongilla* archaeocytes used in **Figure 5C** is  
614 composed of all genes enriched between *Spongilla* archaeocytes and other invertebrate  
615 stem cells. Note that this set includes genes from other species that are linked by SAMap  
616 to the *Spongilla* archeocyte genes. We include genes from other species in the target set  
617 to account for differences in KOG functional annotation coverage between species. As  
618 such, the annotated transcripts from all 7 species are combined to form the background  
619 set. We used a hypergeometric statistical test (Eden et al., 2009) to measure the  
620 enrichment of the KOG terms in the target genes compared to the background genes.

621

### 622 ***Mapping zebrafish and xenopus atlases using existing methods***

623 For benchmarking, we used vertebrate orthologs as determined by EggNOG as input to  
624 Harmony (Korsunsky et al., 2019), Liger (Welch et al., 2019), Seurat (Stuart et al., 2019),  
625 Scanorama (Hie et al., 2019), BBKNN (Polański et al., 2019), which are all run with default  
626 parameters. One-to-one orthologs were selected from one-to-many and many-to-many  
627 orthologs by using the bipartite maximum weight matching algorithm implemented in  
628 *networkx*. When using the one-to-one orthologs as input for SAMap, we ran for only one  
629 iteration. The resulting integrated lower-dimensional coordinates (PCs for Seurat,  
630 Harmony, and Scanorama and non-negative matrix factorization coordinates for Liger)  
631 and stitched graph (BBKNN and SAMap) were all projected into 2D with UMAP (**Figure**  
632 **2 – figure supplement 2A**). The integrated coordinates are used to generate a nearest  
633 neighbor graph using the correlation distance metric, which is then used to compute the

634 alignment scores in **Figure 2 – figure supplement 2B**. The alignment scores for SAMap  
635 and BBKNN are directly computed from their combined graphs.

636

637 ***In-situ hybridization in schistosomes***

638 *S. mansoni* (strain: NMRI) juveniles are retrieved from infected female Swiss Webster  
639 mice (NR-21963) at ~3 weeks post-infection by hepatic portal vein perfusion using 37°C  
640 DMEM supplemented with 5 % heat inactivated FBS. The infected mice are provided by  
641 the NIAID Schistosomiasis Resource Center for distribution through BEI Resources, NIH-  
642 NIAID Contract HHSN272201000005I. In adherence to the Animal Welfare Act and the  
643 Public Health Service Policy on Humane Care and Use of Laboratory Animals, all  
644 experiments with and care of mice are performed in accordance with protocols approved  
645 by the Institutional Animal Care and Use Committees (IACUC) of Stanford University  
646 (protocol approval number 30366). *In situ* hybridization experiments are performed as  
647 described previously (Tarashansky et al., 2019), using riboprobes synthesized from gene  
648 fragments cloned with the listed primers: collagen (Smp\_170340):  
649 GGTGAAGAAGGCTGTTGTGG, ACGATCCCCTTCACTCCTG; tropomyosin  
650 (Smp\_031770): AAGCTGAAGTCGCCTCACTA, CATATGCCTCTTCACGCTGG;  
651 troponin (Smp\_018250): CGTAAACCTGGTCAGAACCG,  
652 ATCCTTTCCAGAGCGT; myosin regulatory light chain (Smp\_132670):  
653 GAGACAGCGAGTAGTGGAGG, TGCCTTCTTGATTGGAGCT; wnt (Smp\_156540):  
654 TGTGGTGATGAAGATGGCAG, CCACGGCCACAACACATATT; frizzled  
655 (Smp\_174350): CGAACAGGCGCATGACAATA, TGCTAGCCTGTTGTCGTGT.

656 **Acknowledgments**

657 We thank D. Wagner and C. Juliano for sharing the data and essential discussions. We  
658 also thank S. Granick, L. Luo, and J. Kebschull for their critical reading of the manuscript.  
659 AJT is a Bio-X Stanford Interdisciplinary Graduate Fellow. This work is supported by a  
660 Beckman Young Investigator Award and an NIH grant (1R35GM138061) to BW.

## 661 References

- 662 Alié, A., Hayashi, T., Sugimura, I., Manuel, M., Sugano, W., Mano, A., Satoh, N., Agata, K., &  
663 Funayama, N. (2015). The ancestral gene repertoire of animal stem cells. *Proceedings of  
664 the National Academy of Sciences*, 112(51), E7093–E7100.  
665 <https://doi.org/10.1073/pnas.1514789112>
- 666 Arendt, D., Bertucci, P. Y., Achim, K., & Musser, J. M. (2019). Evolution of neuronal types and  
667 families. *Current Opinion in Neurobiology*, 56, 144–152.  
668 <https://doi.org/10.1016/j.conb.2019.01.022>
- 669 Arendt, D., Musser, J. M., Baker, C. V. H., Bergman, A., Cepko, C., Erwin, D. H., Pavlicev, M.,  
670 Schlosser, G., Widder, S., Laubichler, M. D., & Wagner, G. P. (2016). The origin and  
671 evolution of cell types. *Nature Reviews Genetics*, 17(12), 744–757.  
672 <https://doi.org/10.1038/nrg.2016.127>
- 673 Barkas, N., Petukhov, V., Nikolaeva, D., Lozinsky, Y., Demharter, S., Khodosevich, K., &  
674 Kharchenko, P. V. (2019). Joint analysis of heterogeneous single-cell RNA-seq dataset  
675 collections. *Nature Methods*, 16(8), 695–698. <https://doi.org/10.1038/s41592-019-0466-z>
- 676 Baron, M., Veres, A., Wolock, S. L., Faust, A. L., Gaujoux, R., Vetere, A., Ryu, J. H., Wagner, B.  
677 K., Shen-Orr, S. S., Klein, A. M., Melton, D. A., & Yanai, I. (2016). A single-cell  
678 transcriptomic map of the human and mouse pancreas reveals inter- and intra-cell  
679 population structure. *Cell Systems*, 3(4), 346–360.e4.  
680 <https://doi.org/10.1016/j.cels.2016.08.011>
- 681 Briggs, J. A., Weinreb, C., Wagner, D. E., Megason, S., Peshkin, L., Kirschner, M. W., & Klein,  
682 A. M. (2018). The dynamics of gene expression in vertebrate embryogenesis at single-cell  
683 resolution. *Science*, 360(6392), eaar5780. <https://doi.org/10.1126/science.aar5780>
- 684 Brunet, T., Fischer, A. H., Steinmetz, P. R., Lauri, A., Bertucci, P., & Arendt, D. (2016). The  
685 evolutionary origin of bilaterian smooth and striated myocytes. *eLife*, 5, e19607.  
686 <https://doi.org/10.7554/eLife.19607>
- 687 Buzgariu, W., Al Haddad, S., Tomczyk, S., Wenger, Y., & Galliot, B. (2015). Multi-functionality  
688 and plasticity characterize epithelial cells in *Hydra*. *Tissue Barriers*, 3(4), e1068908.  
689 <https://doi.org/10.1080/21688370.2015.1068908>
- 690 Cao, C., Lemaire, L. A., Wang, W., Yoon, P. H., Choi, Y. A., Parsons, L. R., Matese, J. C.,  
691 Wang, W., Levine, M., & Chen, K. (2019). Comprehensive single-cell transcriptome lineages  
692 of a proto-vertebrate. *Nature*, 571(7765), 349–354. [https://doi.org/10.1038/s41586-019-1385-y](https://doi.org/10.1038/s41586-019-<br/>693 1385-y)
- 694 Dubaissi, E., Rousseau, K., Lea, R., Soto, X., Nardeosingh, S., Schweickert, A., Amaya, E.,  
695 Thornton, D. J., & Papalopulu, N. (2014). A secretory cell type develops alongside  
696 multiciliated cells, ionocytes and goblet cells, and provides a protective, anti-infective  
697 function in the frog embryonic mucociliary epidermis. *Development*, 141(7), 1514–1525.  
698 <https://doi.org/10.1242/dev.102426>
- 699 Eddy, S. R. (2008). A probabilistic model of local sequence alignment that simplifies statistical  
700 significance estimation. *PLoS Computational Biology*, 4(5), e1000069.  
701 <https://doi.org/10.1371/journal.pcbi.1000069>
- 702 Eden, E., Navon, R., Steinfield, I., Lipson, D., & Yakhini, Z. (2009). GOrilla: A tool for discovery  
703 and visualization of enriched GO terms in ranked gene lists. *BMC Bioinformatics*, 10(1), 48.  
704 <https://doi.org/10.1186/1471-2105-10-48>
- 705 El-Brolosy, M. A., Kontarakis, Z., Rossi, A., Kuenne, C., Günther, S., Fukuda, N., Kikhi, K.,  
706 Boezio, G. L. M., Takacs, C. M., Lai, S.-L., Fukuda, R., Gerri, C., Giraldez, A. J., & Stainier,  
707 D. Y. R. (2019). Genetic compensation triggered by mutant mRNA degradation. *Nature*,  
708 568(7751), 193–197. <https://doi.org/10.1038/s41586-019-1064-z>

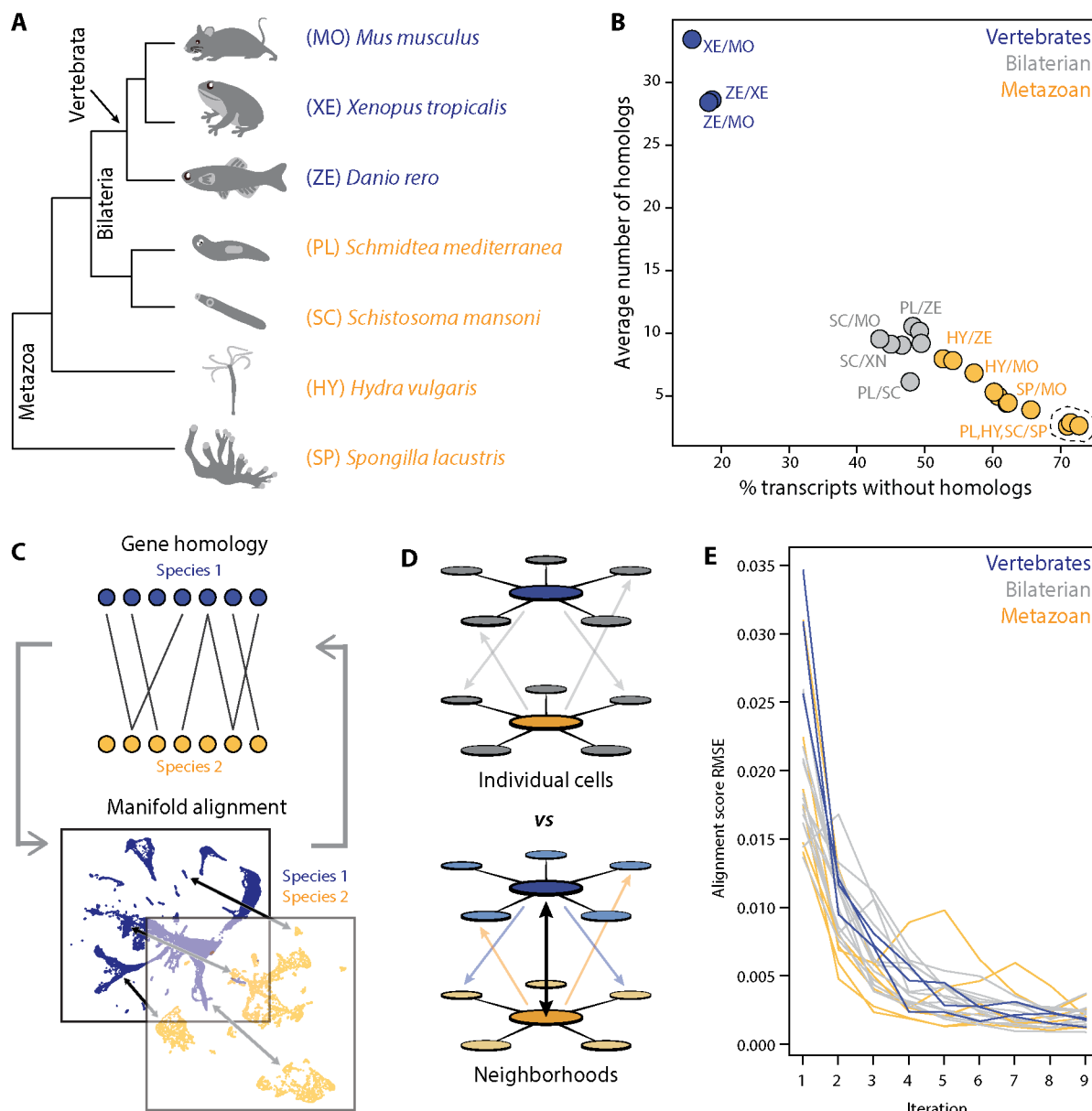
- 709 Fincher, C. T., Wurtzel, O., de Hoog, T., Kravarik, K. M., & Reddien, P. W. (2018). Cell type  
710 transcriptome atlas for the planarian *Schmidtea mediterranea*. *Science*, 360(6391),  
711 eaaq1736. <https://doi.org/10.1126/science.aaq1736>
- 712 Gabaldón, T., & Koonin, E. V. (2013). Functional and evolutionary implications of gene  
713 orthology. *Nature Reviews Genetics*, 14(5), 360–366. <https://doi.org/10.1038/nrg3456>
- 714 Geirsdottir, L., David, E., Keren-Shaul, H., Weiner, A., Bohlen, S. C., Neuber, J., Balic, A.,  
715 Giladi, A., Sheban, F., Dutertre, C.-A., Pfeifle, C., Peri, F., Raffo-Romero, A., Vizioli, J.,  
716 Matiasek, K., Scheiwe, C., Meckel, S., Mätz-Rensing, K., van der Meer, F., ... Prinz, M.  
717 (2019). Cross-Species Single-Cell Analysis Reveals Divergence of the Primate Microglia  
718 Program. *Cell*, 179(7), 1609-1622.e16. <https://doi.org/10.1016/j.cell.2019.11.010>
- 719 Haghverdi, L., Lun, A. T. L., Morgan, M. D., & Marioni, J. C. (2018). Batch effects in single-cell  
720 RNA-sequencing data are corrected by matching mutual nearest neighbors. *Nature  
721 Biotechnology*, 36(5), 421–427. <https://doi.org/10.1038/nbt.4091>
- 722 Hie, B., Bryson, B., & Berger, B. (2019). Efficient integration of heterogeneous single-cell  
723 transcriptomes using Scanorama. *Nature Biotechnology*, 37(6), 685–691.  
724 <https://doi.org/10.1038/s41587-019-0113-3>
- 725 Hu, M., Zheng, X., Fan, C.-M., & Zheng, Y. (2020). Lineage dynamics of the endosymbiotic cell  
726 type in the soft coral *Xenia*. *Nature*, 582(7813), 534–538. <https://doi.org/10.1038/s41586-020-2385-7>
- 727 Huerta-Cepas, J., Serra, F., & Bork, P. (2016). ETE 3: Reconstruction, Analysis, and  
728 Visualization of Phylogenomic Data. *Molecular Biology and Evolution*, 33(6), 1635–1638.  
729 <https://doi.org/10.1093/molbev/msw046>
- 730 Huerta-Cepas, J., Szklarczyk, D., Heller, D., Hernández-Plaza, A., Forsslund, S. K., Cook, H.,  
731 Mende, D. R., Letunic, I., Rattei, T., Jensen, L. J., von Mering, C., & Bork, P. (2019).  
732 eggNOG 5.0: A hierarchical, functionally and phylogenetically annotated orthology resource  
733 based on 5090 organisms and 2502 viruses. *Nucleic Acids Research*, 47(D1), D309–D314.  
734 <https://doi.org/10.1093/nar/gky1085>
- 735 Kalyaanamoorthy, S., Minh, B. Q., Wong, T. K. F., von Haeseler, A., & Jermiin, L. S. (2017).  
736 ModelFinder: Fast model selection for accurate phylogenetic estimates. *Nature Methods*,  
737 14(6), 587–589. <https://doi.org/10.1038/nmeth.4285>
- 738 Korsunsky, I., Millard, N., Fan, J., Slowikowski, K., Zhang, F., Wei, K., Baglaenko, Y., Brenner,  
739 M., Loh, P., & Raychaudhuri, S. (2019). Fast, sensitive and accurate integration of single-  
740 cell data with Harmony. *Nature Methods*, 16(12), 1289–1296.  
741 <https://doi.org/10.1038/s41592-019-0619-0>
- 742 Larroux, C., Luke, G. N., Koopman, P., Rokhsar, D. S., Shimeld, S. M., & Degnan, B. M. (2008).  
743 Genesis and Expansion of Metazoan Transcription Factor Gene Classes. *Molecular Biology  
744 and Evolution*, 25(5), 980–996. <https://doi.org/10.1093/molbev/msn047>
- 745 Laumer, C. E., Hejnol, A., & Giribet, G. (2015). Nuclear genomic signals of the  
746 ‘microturbellarian’ roots of platyhelminth evolutionary innovation. *eLife*, 4, e05503.  
747 <https://doi.org/10.7554/eLife.05503>
- 748 Letunic, I., & Bork, P. (2019). Interactive Tree Of Life (iTOL) v4: Recent updates and new  
749 developments. *Nucleic Acids Research*, 47(W1), W256–W259.  
750 <https://doi.org/10.1093/nar/gkz239>
- 751 Li, P., Sarfati, D. N., Xue, Y., Yu, X., Tarashansky, A. J., Quake, S. R., & Wang, B. (2020).  
752 *Single-cell analysis of Schistosoma mansoni reveals a conserved genetic program  
753 controlling germline stem cell fate* [Preprint]. <https://doi.org/10.1101/2020.07.06.190033>
- 754 Littlewood, D. T. J., & Waeschenbach, A. (2015). Evolution: A Turn Up for the Worms. *Current  
755 Biology*, 25(11), R457–R460. <https://doi.org/10.1016/j.cub.2015.04.012>
- 756 Madeira, F., Park, Y. mi, Lee, J., Buso, N., Gur, T., Madhusoodanan, N., Basutkar, P., Tivey, A.  
757 R. N., Potter, S. C., Finn, R. D., & Lopez, R. (2019). The EMBL-EBI search and sequence  
758

- 759 analysis tools APIs in 2019. *Nucleic Acids Research*, 47(W1), W636–W641.  
760 <https://doi.org/10.1093/nar/gkz268>
- 761 Malkov, Y. A., & Yashunin, D. A. (2020). Efficient and robust approximate nearest neighbor  
762 search using hierarchical navigable small world graphs. *IEEE Transactions on Pattern  
763 Analysis and Machine Intelligence*, 42(4), 824–836.  
764 <https://doi.org/10.1109/TPAMI.2018.2889473>
- 765 Miles, L. B., Darido, C., Kaslin, J., Heath, J. K., Jane, S. M., & Dworkin, S. (2017). Mis-  
766 expression of grainyhead-like transcription factors in zebrafish leads to defects in  
767 enveloping layer (EVL) integrity, cellular morphogenesis and axial extension. *Scientific  
768 Reports*, 7(1), 17607. <https://doi.org/10.1038/s41598-017-17898-7>
- 769 Musser, J. M., Schippers, K. J., Nickel, M., Mizzon, G., Kohn, A. B., Pape, C., Hammel, J. U.,  
770 Wolf, F., Liang, C., Hernández-Plaza, A., Achim, K., Schieber, N. L., Francis, W. R., Vargas  
771 R., S., Kling, S., Renkert, M., Feuda, R., Gaspar, I., Burkhardt, P., ... Arendt, D. (2019).  
772 *Profiling cellular diversity in sponges informs animal cell type and nervous system evolution*  
773 [Preprint]. <https://doi.org/10.1101/758276>
- 774 Nehrt, N. L., Clark, W. T., Radivojac, P., & Hahn, M. W. (2011). Testing the ortholog conjecture  
775 with comparative functional genomic data from mammals. *PLoS Computational Biology*,  
776 7(6), e1002073. <https://doi.org/10.1371/journal.pcbi.1002073>
- 777 Nguyen, L.-T., Schmidt, H. A., von Haeseler, A., & Minh, B. Q. (2015). IQ-TREE: A fast and  
778 effective stochastic algorithm for estimating maximum-likelihood phylogenies. *Molecular  
779 Biology and Evolution*, 32(1), 268–274. <https://doi.org/10.1093/molbev/msu300>
- 780 Pijuan-Sala, B., Griffiths, J. A., Guibentif, C., Hiscock, T. W., Jawaid, W., Calero-Nieto, F. J.,  
781 Mulas, C., Ibarra-Soria, X., Tyser, R. C. V., Ho, D. L. L., Reik, W., Srinivas, S., Simons, B.  
782 D., Nichols, J., Marioni, J. C., & Göttgens, B. (2019). A single-cell molecular map of mouse  
783 gastrulation and early organogenesis. *Nature*, 566(7745), 490–495.  
784 <https://doi.org/10.1038/s41586-019-0933-9>
- 785 Plass, M., Solana, J., Wolf, F. A., Ayoub, S., Misios, A., Glažar, P., Obermayer, B., Theis, F. J.,  
786 Kocks, C., & Rajewsky, N. (2018). Cell type atlas and lineage tree of a whole complex  
787 animal by single-cell transcriptomics. *Science*, 360(6391), eaaq1723.  
788 <https://doi.org/10.1126/science.aaq1723>
- 789 Polański, K., Young, M. D., Miao, Z., Meyer, K. B., Teichmann, S. A., & Park, J.-E. (2019).  
790 BBKNN: Fast batch alignment of single cell transcriptomes. *Bioinformatics*, btz625.  
791 <https://doi.org/10.1093/bioinformatics/btz625>
- 792 Prince, V. E., & Pickett, F. B. (2002). Splitting pairs: The diverging fates of duplicated genes.  
793 *Nature Reviews Genetics*, 3(11), 827–837. <https://doi.org/10.1038/nrg928>
- 794 Reddien, P. W. (2018). The Cellular and Molecular Basis for Planarian Regeneration. *Cell*,  
795 175(2), 327–345. <https://doi.org/10.1016/j.cell.2018.09.021>
- 796 Regev, A., Teichmann, S. A., Lander, E. S., Amit, I., Benoist, C., Birney, E., Bodenmiller, B.,  
797 Campbell, P., Carninci, P., Clatworthy, M., Clevers, H., Deplancke, B., Dunham, I.,  
798 Eberwine, J., Eils, R., Enard, W., Farmer, A., Fugger, L., Göttgens, B., ... Human Cell Atlas  
799 Meeting Participants. (2017). The Human Cell Atlas. *eLife*, 6, e27041.  
800 <https://doi.org/10.7554/eLife.27041>
- 801 Scimone, M. L., Cote, L. E., & Reddien, P. W. (2017). Orthogonal muscle fibres have different  
802 instructive roles in planarian regeneration. *Nature*, 551(7682), 623–628.  
803 <https://doi.org/10.1038/nature24660>
- 804 Sebé-Pedrós, A., Chomsky, E., Pang, K., Lara-Astiaso, D., Gaiti, F., Mukamel, Z., Amit, I.,  
805 Hejnol, A., Degnan, B. M., & Tanay, A. (2018). Early metazoan cell type diversity and the  
806 evolution of multicellular gene regulation. *Nature Ecology & Evolution*, 2(7), 1176–1188.  
807 <https://doi.org/10.1038/s41559-018-0575-6>
- 808 Shafer, M. E. R. (2019). Cross-Species Analysis of Single-Cell Transcriptomic Data. *Frontiers in  
809 Cell and Developmental Biology*, 7, 175. <https://doi.org/10.3389/fcell.2019.00175>

- 810 Siebert, S., Farrell, J. A., Cazet, J. F., Abeykoon, Y., Primack, A. S., Schnitzler, C. E., & Juliano,  
811 C. E. (2019). Stem cell differentiation trajectories in *Hydra* resolved at single-cell resolution.  
812 *Science*, 365(6451), eaav9314. <https://doi.org/10.1126/science.aav9314>
- 813 Stamboulian, M., Guerrero, R. F., Hahn, M. W., & Radivojac, P. (2020). The ortholog conjecture  
814 revisited: The value of orthologs and paralogs in function prediction. *Bioinformatics*,  
815 36(Supplement\_1), i219–i226. <https://doi.org/10.1093/bioinformatics/btaa468>
- 816 Stuart, T., Butler, A., Hoffman, P., Hafemeister, C., Papalexi, E., Mauck, W. M., Hao, Y.,  
817 Stoeckius, M., Smibert, P., & Satija, R. (2019). Comprehensive Integration of Single-Cell  
818 Data. *Cell*, 177(7), 1888–1902.e21. <https://doi.org/10.1016/j.cell.2019.05.031>
- 819 Studer, R. A., & Robinson-Rechavi, M. (2009). How confident can we be that orthologs are  
820 similar, but paralogs differ? *Trends in Genetics*, 25(5), 210–216.  
821 <https://doi.org/10.1016/j.tig.2009.03.004>
- 822 Tarashansky, A. J., Xue, Y., Li, P., Quake, S. R., & Wang, B. (2019). Self-assembling manifolds  
823 in single-cell RNA sequencing data. *eLife*, 8, e48994. <https://doi.org/10.7554/eLife.48994>
- 824 Tatusov, R. L., Fedorova, N. D., Jackson, J. D., Jacobs, A. R., Kiryutin, B., Koonin, E. V.,  
825 Krylov, D. M., Mazumder, R., Mekhedov, S. L., Nikolskaya, A. N., Rao, B. S., Smirnov, S.,  
826 Sverdlov, A. V., Vasudevan, S., Wolf, Y. I., Yin, J. J., & Natale, D. A. (2003). The COG  
827 database: An updated version includes eukaryotes. *BMC Bioinformatics*, 14.
- 828 Tosches, M. A., & Arendt, D. (2013). The bilaterian forebrain: An evolutionary chimaera. *Current  
829 Opinion in Neurobiology*, 23(6), 1080–1089. <https://doi.org/10.1016/j.conb.2013.09.005>
- 830 Tosches, M. A., Yamawaki, T. M., Naumann, R. K., Jacobi, A. A., Tushev, G., & Laurent, G.  
831 (2018). Evolution of pallium, hippocampus, and cortical cell types revealed by single-cell  
832 transcriptomics in reptiles. *Science*, 360(6391), 881–888.  
833 <https://doi.org/10.1126/science.aar4237>
- 834 Traag, V. A., Waltman, L., & van Eck, N. J. (2019). From Louvain to Leiden: Guaranteeing well-  
835 connected communities. *Scientific Reports*, 9(1), 5233. [https://doi.org/10.1038/s41598-019-41695-z](https://doi.org/10.1038/s41598-019-<br/>836 41695-z)
- 837 Wagner, D. E., Weinreb, C., Collins, Z. M., Briggs, J. A., Megason, S., & Klein, A. M. (2018).  
838 Single-cell mapping of gene expression landscapes and lineage in the zebrafish embryo.  
839 *Science*, 360(6392), 981–987.
- 840 Wang, B., Lee, J., Li, P., Saberi, A., Yang, H., Liu, C., Zhao, M., & Newmark, P. A. (2018). Stem  
841 cell heterogeneity drives the parasitic life cycle of *Schistosoma mansoni*. *eLife*, 7, e35449.  
842 <https://doi.org/10.7554/eLife.35449>
- 843 Weir, K., Dupre, C., van Giesen, L., Lee, A. S.-Y., & Bellono, N. W. (2020). A molecular filter for  
844 the cnidarian stinging response. *eLife*, 9, e57578. <https://doi.org/10.7554/eLife.57578>
- 845 Welch, J. D., Kozareva, V., Ferreira, A., Vanderburg, C., Martin, C., & Macosko, E. Z. (2019).  
846 Single-Cell Multi-omic Integration Compares and Contrasts Features of Brain Cell Identity.  
847 *Cell*, 177(7), 1873–1887.e17. <https://doi.org/10.1016/j.cell.2019.05.006>
- 848 Wendt, G. R., & Collins, J. J. (2016). Schistosomiasis as a disease of stem cells. *Current  
849 Opinion in Genetics & Development*, 40, 95–102. <https://doi.org/10.1016/j.gde.2016.06.010>
- 850 Wendt, G. R., Collins, J. N., Pei, J., Pearson, M. S., Bennett, H. M., Loukas, A., Berriman, M.,  
851 Grishin, N. V., & Collins, J. J. (2018). Flatworm-specific transcriptional regulators promote  
852 the specification of tegumental progenitors in *Schistosoma mansoni*. *eLife*, 7, e33221.  
853 <https://doi.org/10.7554/eLife.33221>
- 854 Wolf, F. A., Angerer, P., & Theis, F. J. (2018). SCANPY: Large-scale single-cell gene  
855 expression data analysis. *Genome Biology*, 19(1), 15. [https://doi.org/10.1186/s13059-017-1382-0](https://doi.org/10.1186/s13059-017-<br/>856 1382-0)
- 857 Wong, E., Mölter, J., Anggono, V., Degnan, S. M., & Degnan, B. M. (2019). Co-expression of  
858 synaptic genes in the sponge *Amphimedon queenslandica* uncovers ancient neural  
859 submodules. *Scientific Reports*, 9(1), 15781. <https://doi.org/10.1038/s41598-019-51282-x>

- 860 Yan, K.-K., Wang, D., Rozowsky, J., Zheng, H., Cheng, C., & Gerstein, M. (2014). OrthoClust:  
861 An orthology-based network framework for clustering data across multiple species. *Genome*  
862 *Biology*, 15(8), R100. <https://doi.org/10.1186/gb-2014-15-8-r100>
- 863 Zeng, A., Li, H., Guo, L., Gao, X., McKinney, S., Wang, Y., Yu, Z., Park, J., Semerad, C., Ross,  
864 E., Cheng, L.-C., Davies, E., Lei, K., Wang, W., Perera, A., Hall, K., Peak, A., Box, A., &  
865 Sánchez Alvarado, A. (2018). Prospectively Isolated Tetraspanin+ Neoblasts Are Adult  
866 Pluripotent Stem Cells Underlying Planaria Regeneration. *Cell*, 173(7), 1593-1608.e20.  
867 <https://doi.org/10.1016/j.cell.2018.05.006>

868 **Figures**

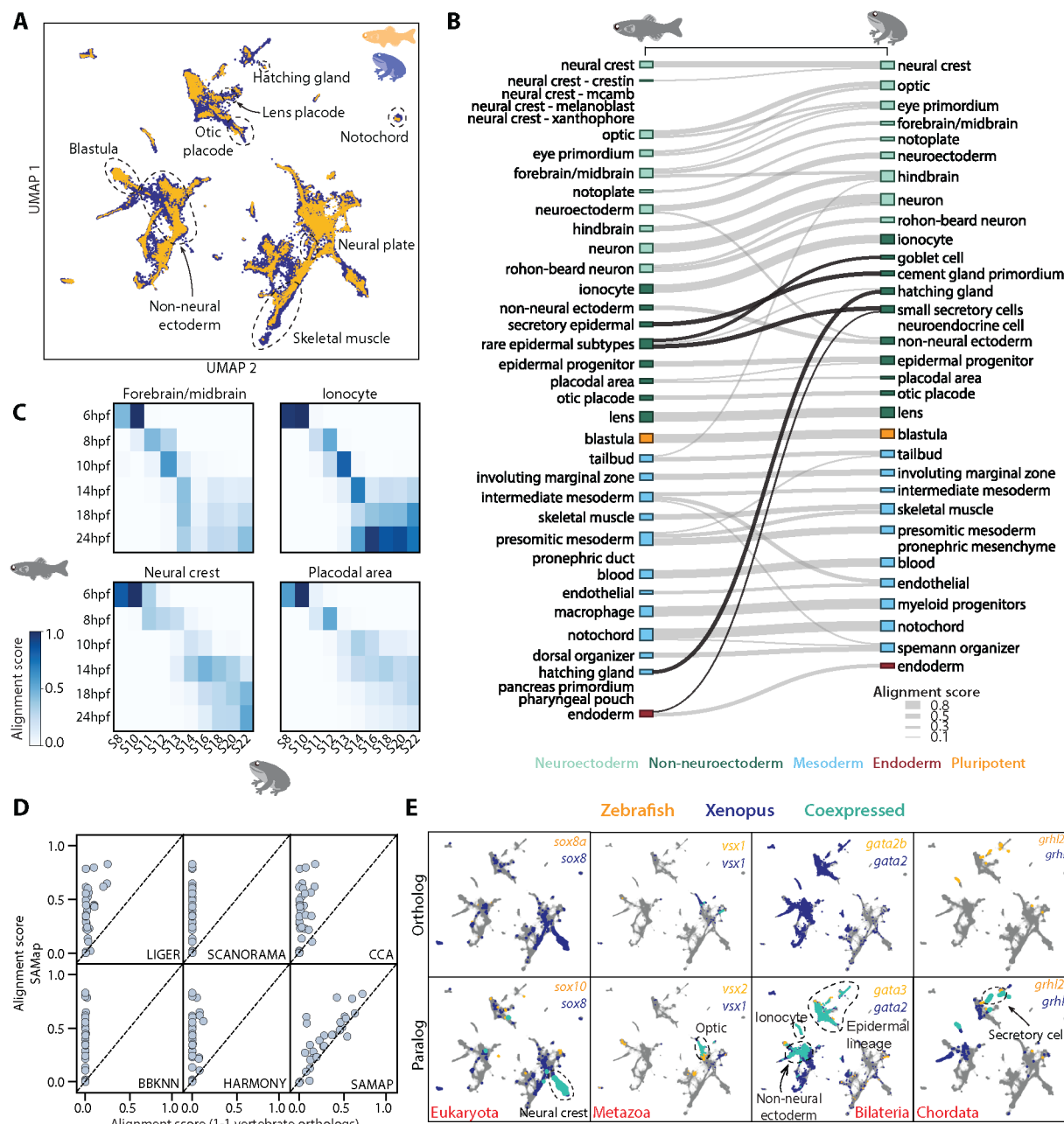


869

870 **Figure 1: SAMap addresses challenges in mapping cell atlases of distantly related**  
 871 **species.** (A) Schematic showing the phylogenetic relationships among 7 species  
 872 analyzed. (B) Challenges in mapping single-cell transcriptomes. Gene duplications cause  
 873 large numbers of homologs per gene, determined by reciprocal BLAST (cut-off: e-value  
 874  $< 10^{-6}$ ), and frequent gene losses and the acquisition of new genes results in large

875 fractions of transcriptomes lacking homology, which limits the amount of information  
876 comparable across species. (C) SAMap workflow. Homologous gene pairs initially  
877 weighted by protein sequence similarity are used to align the manifolds, low dimensional  
878 representations of the cell atlases. Gene-gene correlations calculated from the aligned  
879 manifolds are used to update the edge weights in the bipartite graph, which are then used  
880 to improve manifold alignment. (D) Mutual nearest neighborhoods improve the detection  
881 of cross-species mutual nearest neighbors by connecting cells that target one other's  
882 within-species neighborhoods. (E) Convergence of SAMap is evaluated by the root mean  
883 square error (RMSE) of the alignment scores between mapped clusters in adjacent  
884 iterations for all 21 pairwise comparisons of the 7 species.

885

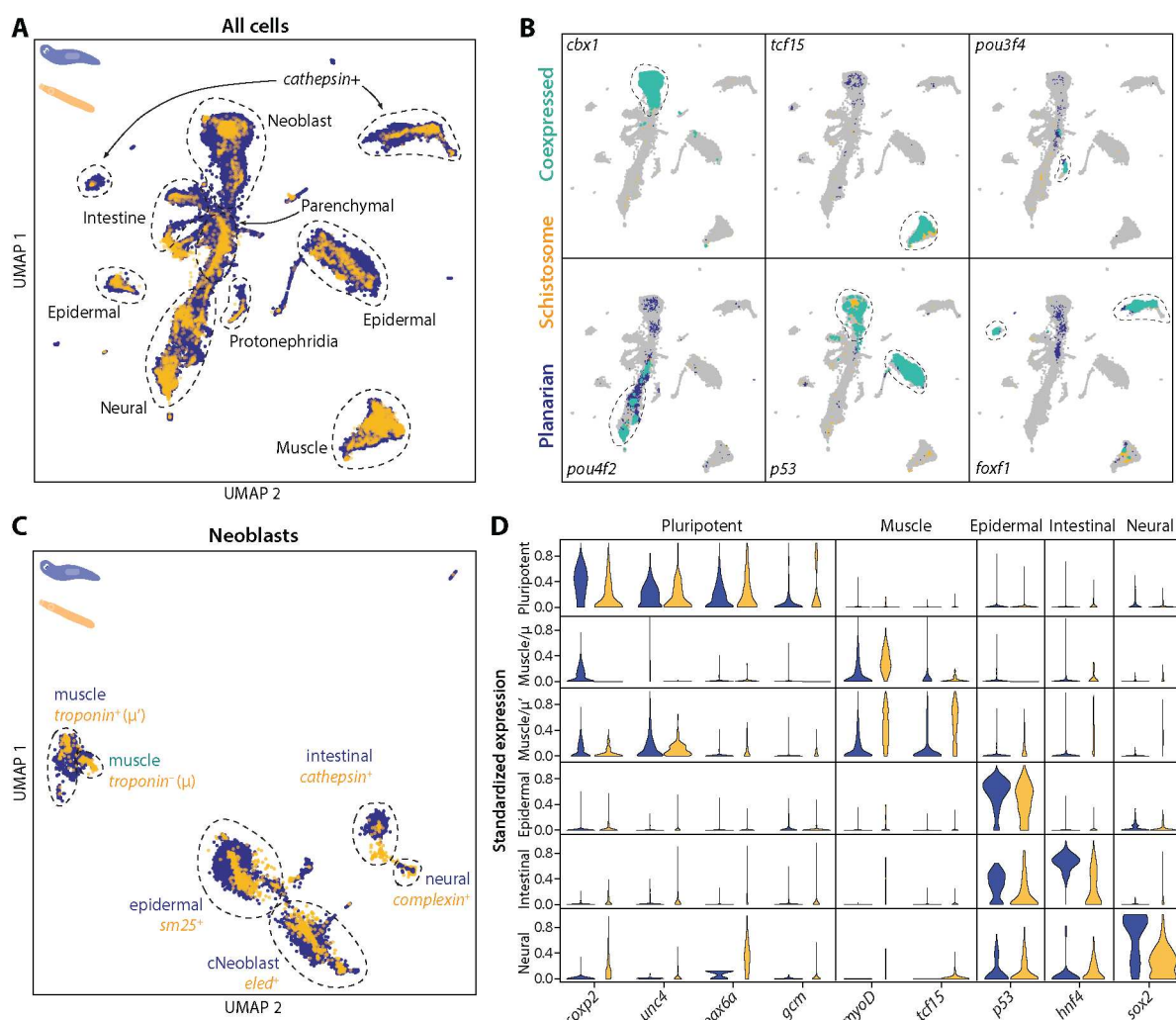


886

887 **Figure 2: SAMap successfully maps *D. rerio* and *X. tropicalis* atlases and reveals**  
 888 **prevalent paralog substitutions.** (A) UMAP projection of the combined zebrafish  
 889 (yellow) and *Xenopus* (blue) manifolds, with example cell types circled. (B) Sankey plot  
 890 summarizing the cell type mappings. Edges with alignment score < 0.1 are omitted. Edges  
 891 that connect developmentally distinct secretory cell types are highlighted in black. (C)

892 Heatmaps of alignment scores between developmental time points for ionocyte,  
893 forebrain/midbrain, placodal, and neural crest lineages. X-axis: zebrafish. Y-axis:  
894 *Xenopus*. (D) SAMap alignment scores compared to those of benchmarking methods  
895 using one-to-one vertebrate orthologs as input. Each dot represents a cell type pair  
896 supported by ontogeny annotations. (E) Expression of orthologous (left) and paralogous  
897 (right) gene pairs overlaid on the combined UMAP projection. Expressing cells are color-  
898 coded by species, with those that are connected across species colored cyan. Cells with  
899 no expression are shown in gray. More examples are provided in **Figure 2 – figure**  
900 **supplement 3.**

901



902

903 **Figure 3: SAMap transfers cell type information from a well-annotated organism**

904 **(planarian *S. mediterranea*) to its less-studied cousin (schistosome *S. mansoni*)**

905 **and identifies parallel stem cell compartments.** (A) UMAP projection of the combined

906 manifolds. Tissue type annotations are adopted from the *S. mediterranea* atlas (Fincher

907 et al., 2018). The schistosome atlas was collected from juvenile worms, which we found

908 to contain neoblasts with an abundance comparable to that of planarian neoblasts (Li et

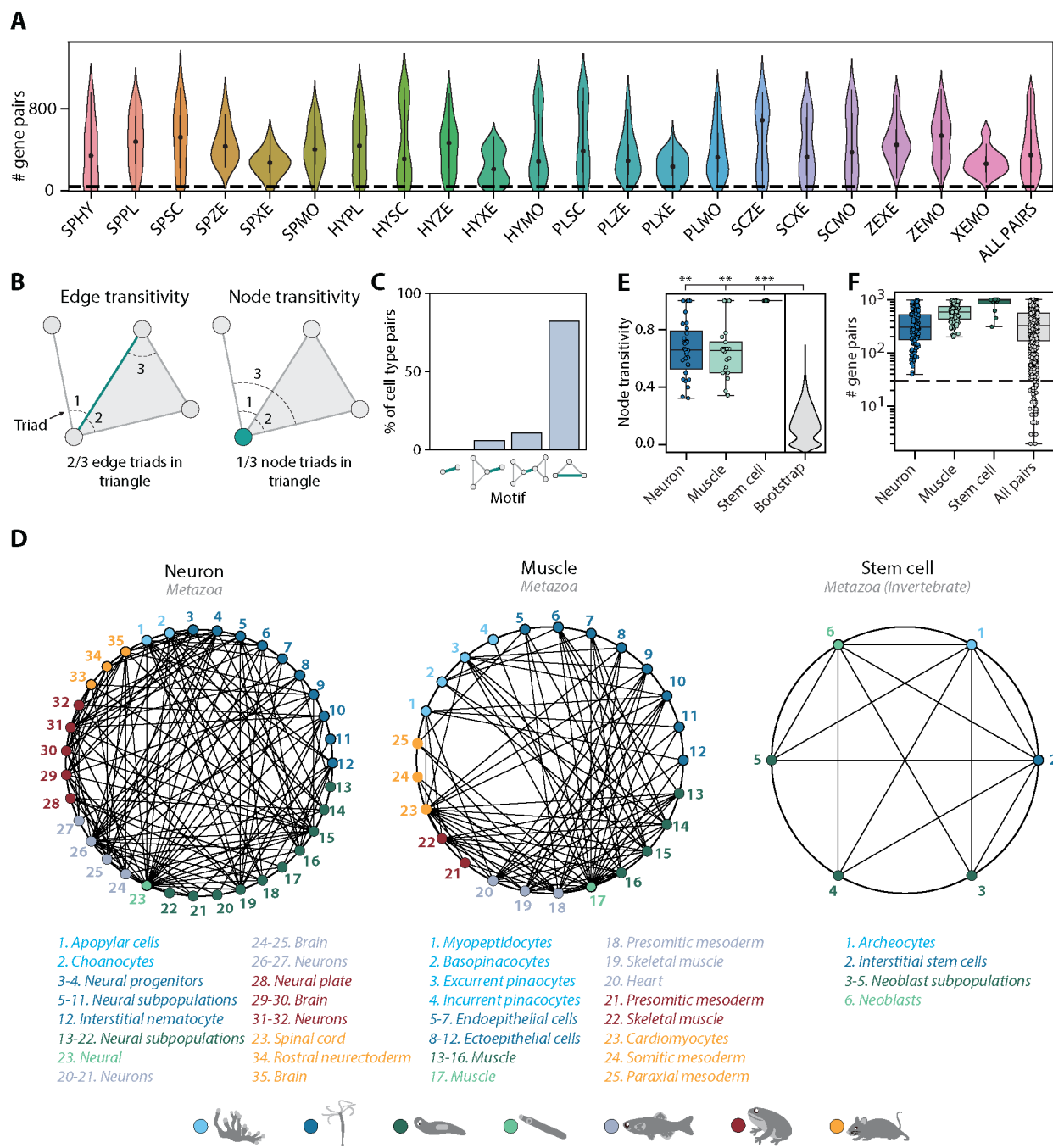
909 al., 2020). (B) Overlapping expressions of selected tissue-specific TFs with expressing

910 cell types circled. (C) UMAP projection of the aligned manifolds showing planarian and

911 schistosome neoblasts, with homologous subpopulations circled. Planarian neoblast data

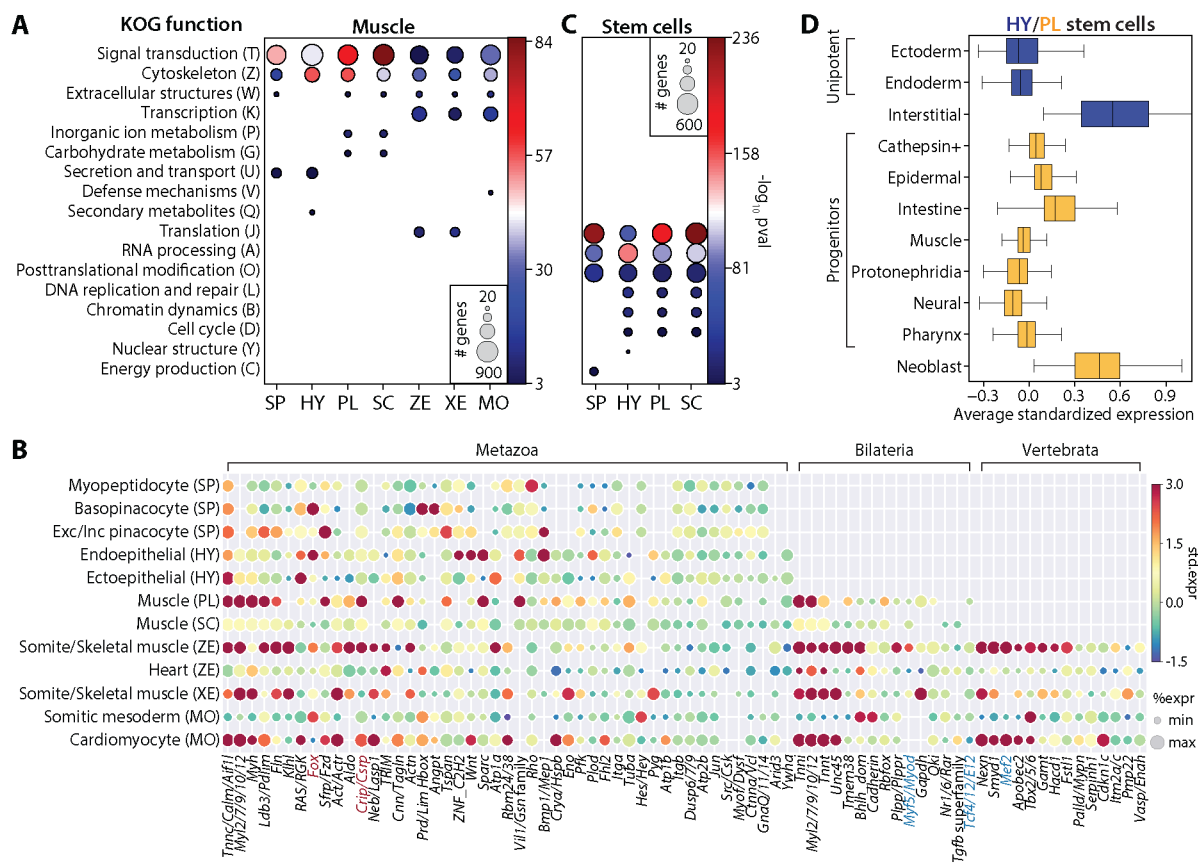
912 is from (Zeng et al., 2018), and cNeoblasts correspond to the Nb2 population, which are  
913 pluripotent cells that can rescue neoblast-depleted planarians in transplantation  
914 experiments. (D) Distributions of conserved TF expressions in each neoblast  
915 subpopulation. Expression values are  $k$ -nearest-neighbor averaged and standardized,  
916 with negative values set to zero. Blue: planarian; yellow: schistosome.

917



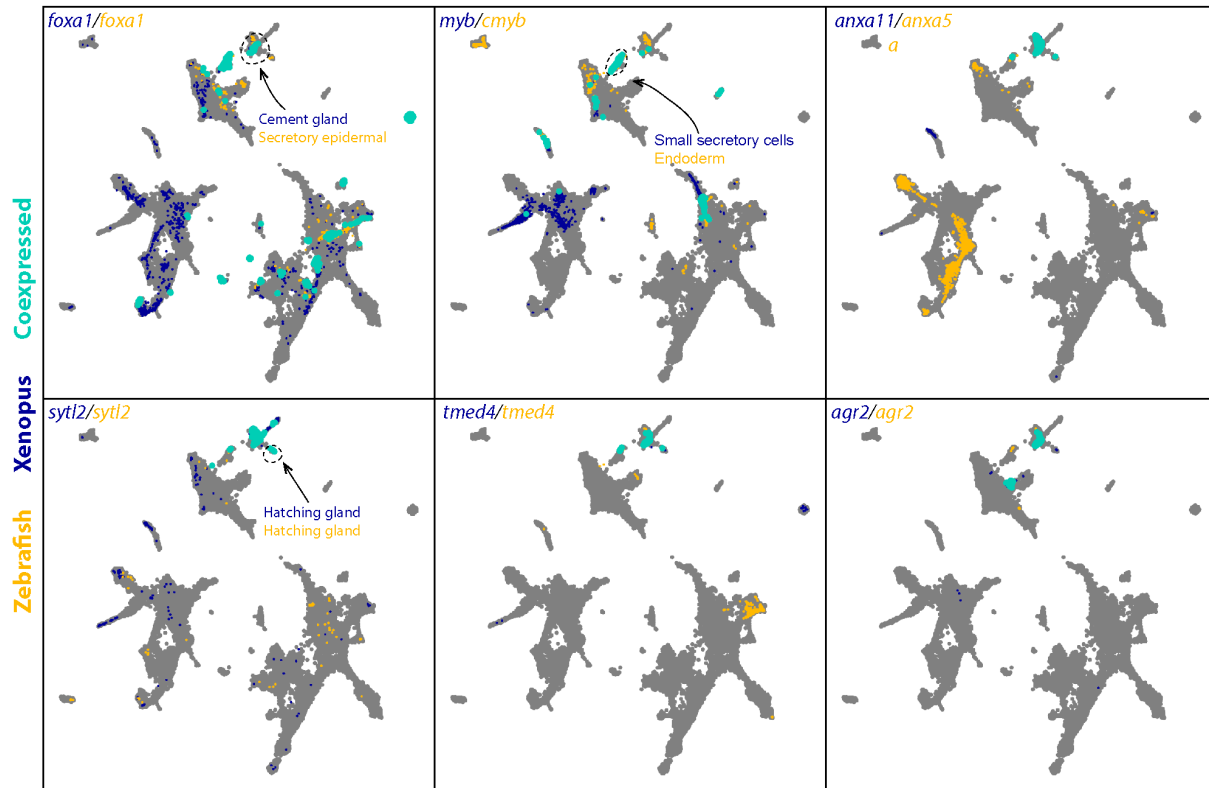
919 **Figure 4: Mapping evolutionarily distant species identifies densely connected cell**  
 920 **type groups.** (A) Violin plots showing the number of enriched gene pairs in cell type  
 921 mappings from all 21 pairwise mappings between the 7 species. 87% of cell type  
 922 mappings have greater than 40 enriched gene pairs (dotted line). Species acronyms are

923 the same as in **Figure 1A**. (B) Schematic illustrating edge (left) and node (right)  
924 transitivities, defined as the fraction of triads (set of three connected nodes) in closed  
925 triangles. (C) The percentage of cell type pairs that are topologically equivalent to the  
926 green edge in each illustrated motif. (D) Network graphs showing highly connected cell  
927 type families. Each node represents a cell type, color-coded by species (detailed  
928 annotations are provided in **Supplementary Table 5**). Mapped cell types are connected  
929 with an edge. (E) Boxplot showing the median and interquartile ranges of node  
930 transitivities for highly connected cell type groups. For all box plots, the whiskers denote  
931 the maximum and minimum observations. The average node transitivity per group is  
932 compared to a bootstrapped null transitivity distribution, generated by repeatedly  
933 sampling subsets of nodes in the cell type graph and calculating their transitivities. \*p <  
934  $5 \times 10^{-3}$ , \*\* p <  $5 \times 10^{-5}$ , \*\*\*p <  $5 \times 10^{-7}$ . (F) Boxplot showing the median and interquartile  
935 ranges of the number of enriched gene pairs in highly connected cell type groups. All cell  
936 type connections in these groups have at least 40 enriched gene pairs (dotted line).



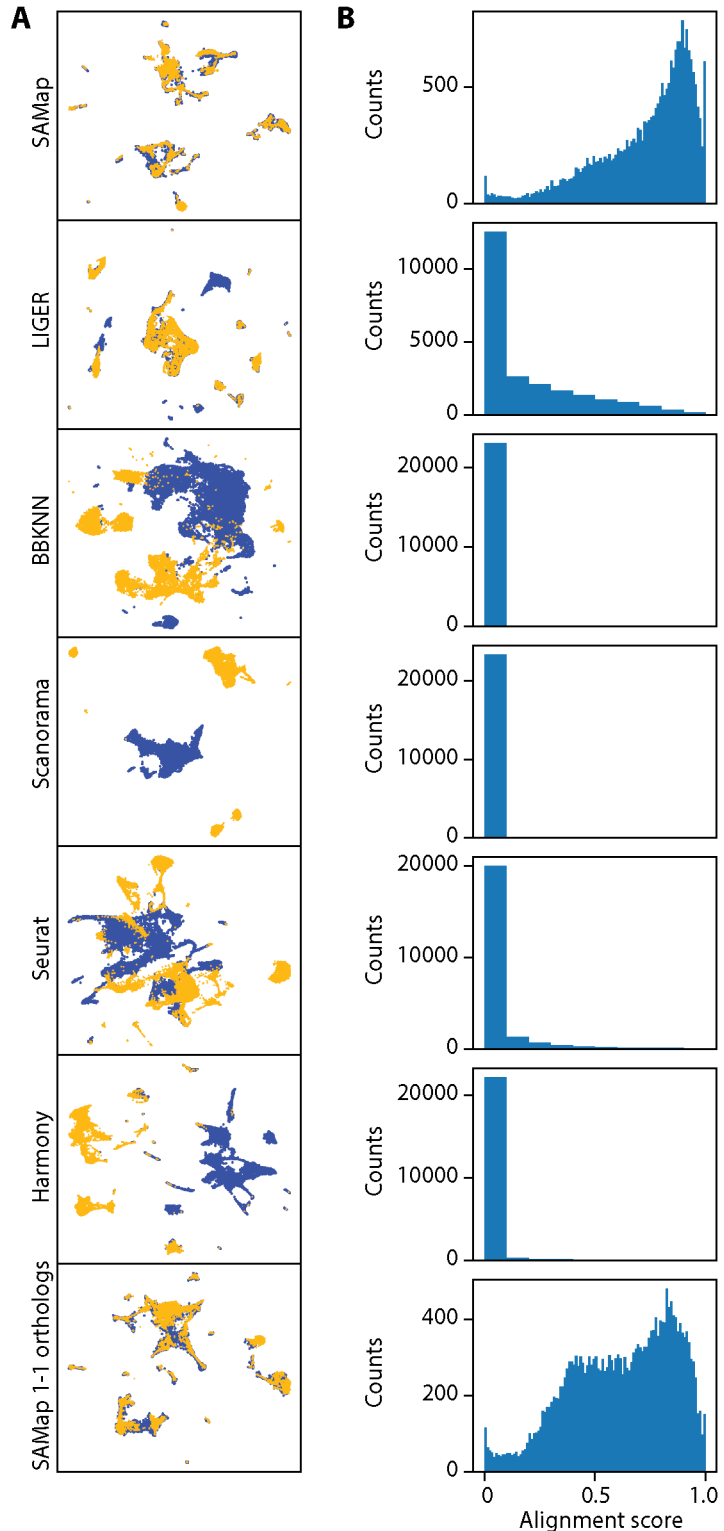
949 interquartile ranges of the mean standardized expressions of genes in hydra and  
950 planarian stem cells/progenitors that are conserved across all invertebrate species in this  
951 study. Planarian progenitors: *piwi*<sup>+</sup> cells that cluster with differentiated tissues in Fincher  
952 et al. (Fincher et al., 2018). Neoblasts: cluster 0 in Fincher et al. (Fincher et al., 2018) that  
953 does not express any tissue-specific markers.

954



956 **Figure 2 – figure supplement 1: Expression of selected genes enriched in *D. rerio***  
957 **and *X. tropicalis* secretory cell types.** Expressions of orthologous gene pairs linked by  
958 SAMap are overlaid on the combined UMAP projection. Expressing cells are color-coded  
959 by species, with those connected across species colored cyan. Cells with no expression  
960 are shown in gray. The mapped secretory cell types are highlighted with circles.

961



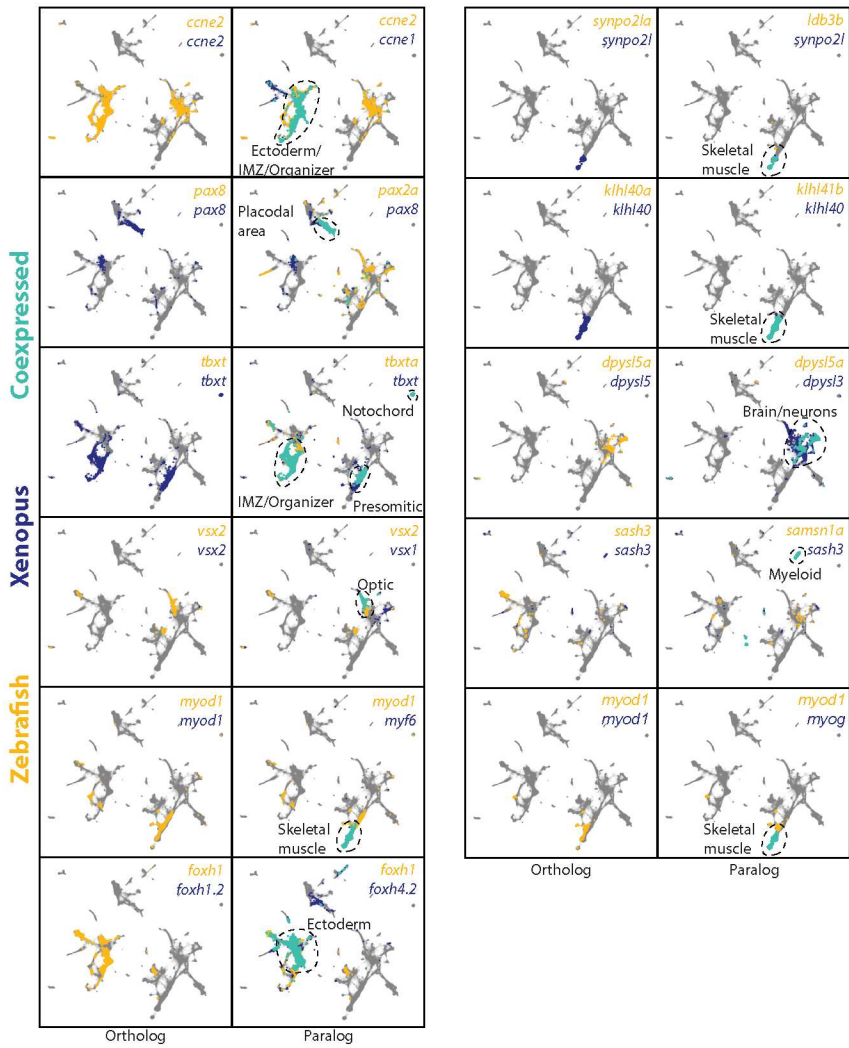
962

963 **Figure 2 – figure supplement 2: Existing methods failed to map *D. rerio* and *X.***

964 ***tropicalis* atlases.** (A) UMAP projections of the integration results from SAMap using the

965 full homology graph, compared to Liger, BBKNN, Scanorama, Seurat, Harmony, and  
966 SAMap using 1-1 orthologs. For fair comparisons, all methods were run on the *D. rerio*  
967 and *X. tropicalis* atlases subsampled to approximately 15,000 cells to satisfy  
968 computational constraints of Seurat and Liger. (B) Distribution of alignment scores  
969 between individual cells.

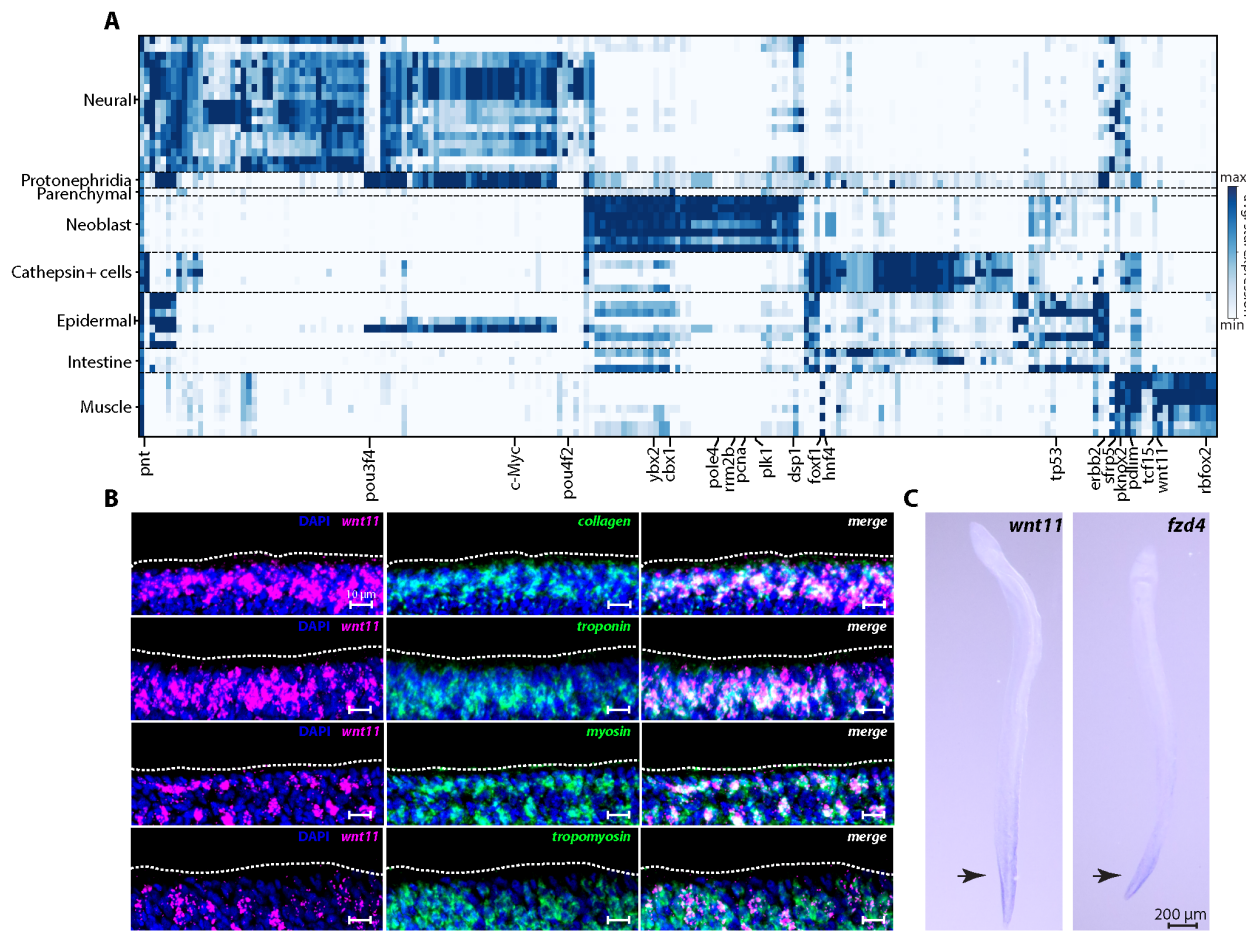
970



971

972 **Figure 2 – figure supplement 3: Representative examples of paralog substitution**  
973 **events in *D. rerio* and *X. tropicalis* atlases.** Expressions of orthologous and paralogous  
974 genes are overlaid on the combined UMAP projection. Expressing cells are color-  
975 coded by species, with those that are connected across species colored in cyan. Cells  
976 with no expression are shown in gray.

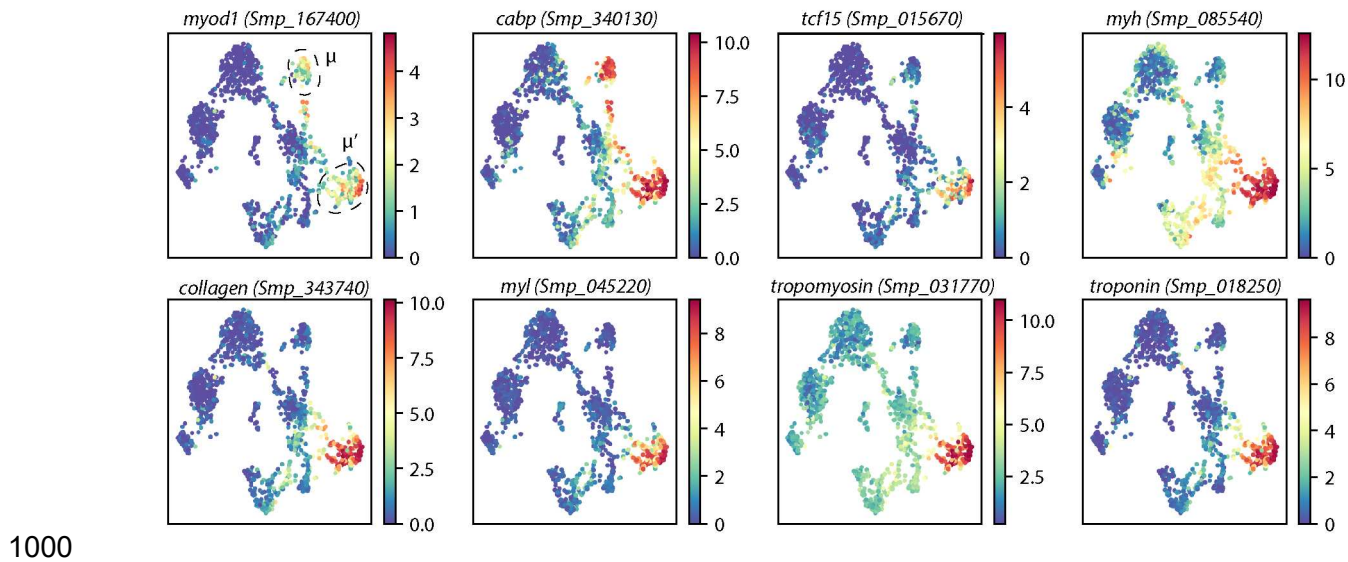
977



978

979 **Figure 3 – figure supplement 1: SAMap-linked gene pairs that are enriched in cell**  
980 **type pairs between *S. mediterranea* and *S. mansoni*.** (A) Rows: linked cell types.  
981 Schistosome cell types correspond to leiden clusters. Columns: genes linked by SAMap  
982 with overlapping eukaryotic EggNOG orthology groups. We calculate the average  
983 standardized expression of each gene in an orthology group for its corresponding cell  
984 type in a particular pair and report the highest expression. A selected set of orthology  
985 groups corresponding to transcriptional regulators are labeled. (B) Fluorescence *in situ*  
986 hybridization shows the co-expression of *wnt* (Smp\_156540) and a panel of muscle  
987 markers (*collagen*, *troponin*, *myosin* and *tropomyosin*) in *S. mansoni* juveniles. The body  
988 wall muscles are expected to be located close to the parasite surface (dashed outline).

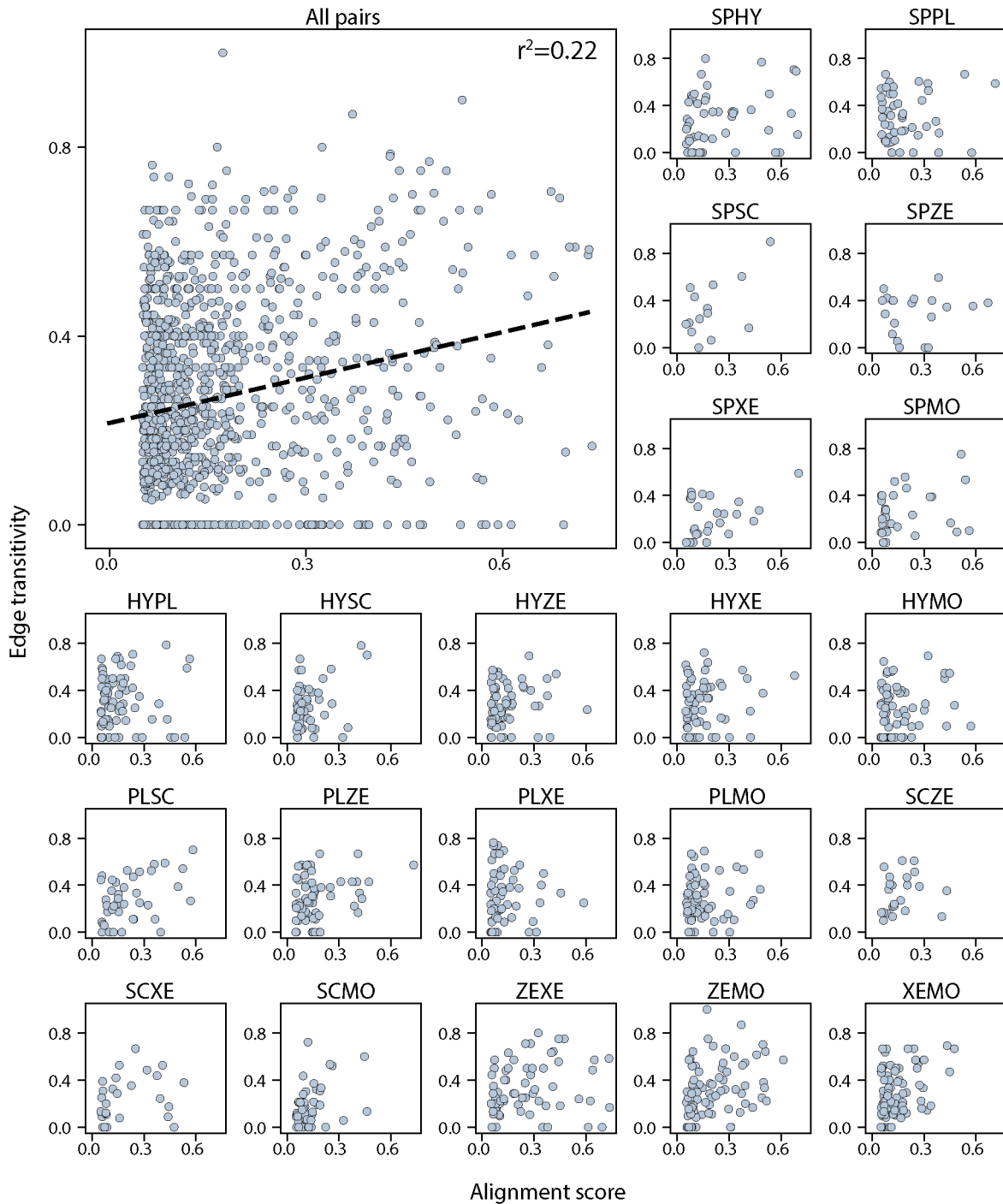
989 The images are maximum intensity projections constructed from ~10 confocal slices with  
990 optimal axial spacing recommended by the Zen software collected on a Zeiss LSM 800  
991 confocal microscope using a 40× (N.A. = 1.1, working distance = 0.62 mm) water-  
992 immersion objective (LD C-Apochromat Corr M27). (C) Whole mount *in situ* hybridization  
993 images showing that the expression of *wnt* and *frizzled* (Smp\_174350) are concentrated  
994 in the parasite tail (arrows) with decreasing gradients extending anteriorly. In planarian  
995 muscles, Wnt genes provide the positional cues for setting up the body plan during  
996 regeneration (Scimone et al., 2017; Reddien, 2018). The presence of an anterior-  
997 posterior expression gradient of *wnt* and *frizzled* in muscles of schistosome juveniles  
998 suggests that they may have similar functional roles in patterning during development.  
999



1000

1001 **Figure 3 – figure supplement 2: Schistosome neoblasts express canonical muscle**  
1002 **markers in muscle progenitors.** UMAP projections of schistosome neoblasts with gene  
1003 expressions overlaid.  $\mu$  and  $\mu'$  cells are circled. Colormap: expression in units of  $\log_2(D +$   
1004 1). For visualization, expression was smoothed via nearest-neighbor averaging using  
1005 SAM. Note that *myod1* and *cabp* are expressed in both presumptive muscle progenitor  
1006 populations, whereas all other markers are enriched in  $\mu'$  cells. All genes displayed are  
1007 also expressed in fully differentiated muscle tissues.

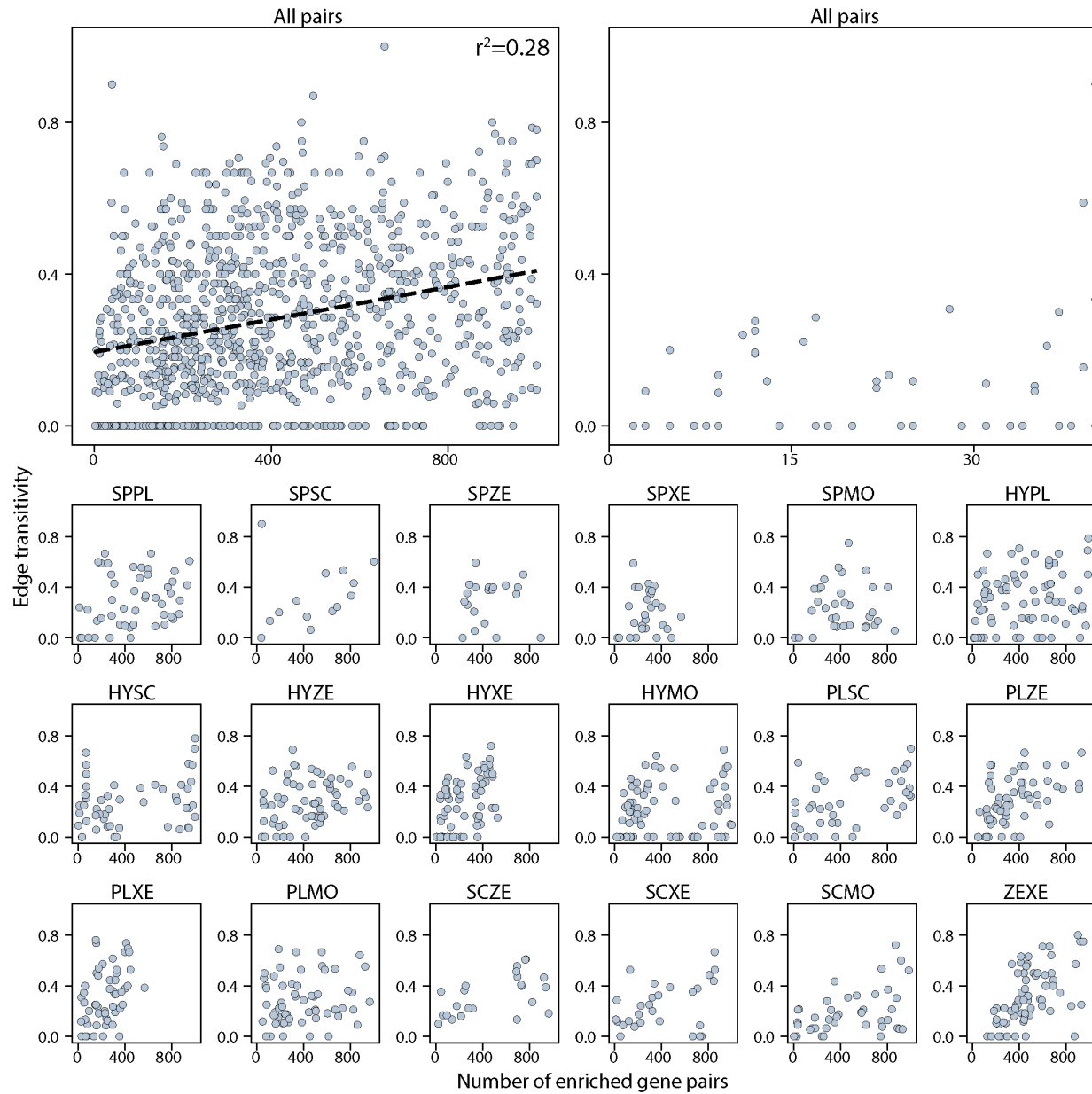
1008



1013 correlation coefficient reported at the top. Alignment scores and edge transitivity for

1014 individual species pairs are shown in the remaining subplots.

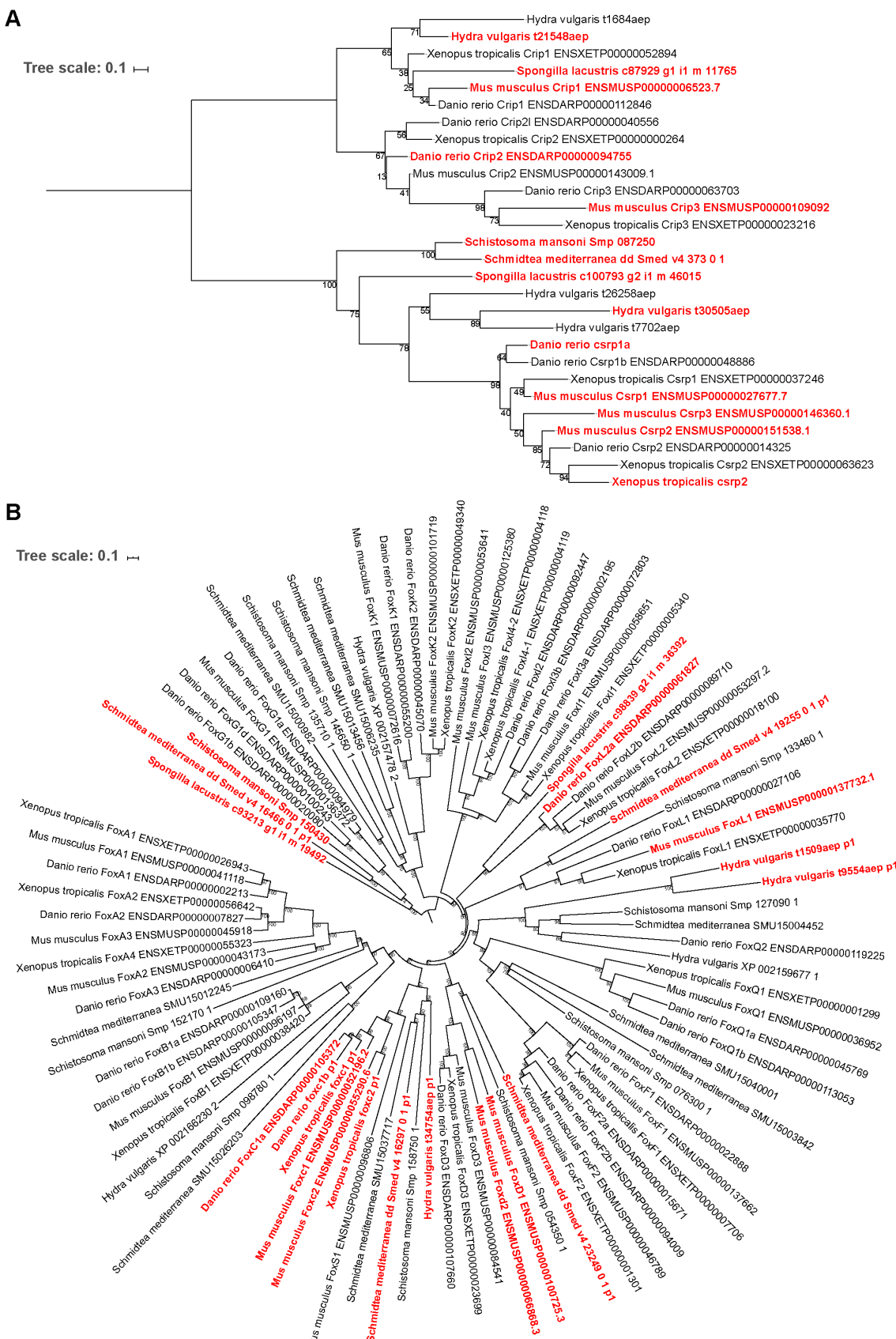
1015



1016

1017 **Figure 4 – figure supplement 2: Number of enriched gene pairs are mostly**  
1018 **independent of edge transitivity.** Top left: The edge transitivity is plotted against the  
1019 number of enriched gene pairs for all cell type pairs in the connectivity graph. Dotted line:  
1020 the linear best fit, with the Pearson correlation coefficient reported at the top. Top right:  
1021 magnified view of the mapped cell type pairs supported by small numbers of gene pairs

1022 (<40) to show those edges have low transitivity scores (<0.4). The sublots below show  
1023 the number of enriched gene pairs and edge transitivity for individual species pairs.  
1024



1026 **Figure 5 – figure supplement 1: Phylogenetic reconstruction of animal contractile  
1027 cell transcriptional regulators.** Trees depict *Csrp/Crip* (A) and Fox group I (B) gene  
1028 families. Genes labelled red are enriched in at least one contractile gene pair identified  
1029 via SAMap. Support values indicate bootstrap support from 1,000 nonparametric (*Csrp*)  
1030 or ultrafast (*Fox*) bootstrap replicates. Besides these two transcriptional regulators,  
1031 contractile cells in all seven species were found to be also enriched for transcription  
1032 factors from the C2H2 Zinc Finger, Lim Homeobox, and Paired Homeobox families,  
1033 although in different cell types we found enrichment of a number of distinct orthologs.  
1034 Whether this reflects an ancestral role for these transcription factor families in regulating  
1035 contractility or their independent evolution will require additional taxonomic sampling and  
1036 broader coverage of muscle cell diversity to resolve.

1037 **Supplementary table captions**

1038

1039 **Supplementary Table 1: Cell atlas metadata and cell annotations.** Metadata includes  
1040 the number of cells, number of transcripts in the transcriptome, median number of  
1041 transcripts detected per cell, the reference transcriptome used in this study, database  
1042 through which the transcriptomes are provided, technology used for constructing the cell  
1043 atlases, atlas data accessions, processing notes, and references. Leiden clusters and  
1044 cell type annotations are reported for cells in each atlas. The Zebrafish and *Xenopus*  
1045 tables include both the original cell type annotations and those used in this study. *D. rerio*,  
1046 *X. tropicalis*, and mouse annotations include developmental stages.

1047

1048 **Supplementary Table 2: Cell type annotations for the zebrafish-*Xenopus* mapping.**  
1049 Correspondence between the cell type annotations provided in the original study (Briggs  
1050 et al., 2018; Wagner et al., 2018) and corresponding annotations used in this study is  
1051 provided for both *D. rerio* and *X. tropicalis* atlases.

1052

1053 **Supplementary Table 3: Identified paralogs with greater expression similarity than**  
1054 **orthologs in the zebrafish-*Xenopus* mapping.** Each row contains a pair of vertebrate-  
1055 orthologous genes and a corresponding pair of eukaryotic paralogs with higher correlation  
1056 in expression compared to the orthologs, the expression correlations for ortholog and  
1057 paralog pairs, the difference between their correlations, and whether the paralogs are  
1058 considered as a paralog substitution (defined as when the substituted ortholog is either

1059 absent or lowly-expressed with no cell-type specificity). Highlighted rows are shown in

1060 **Figure 2E and Figure 2 – figure supplement 3.**

1061

1062 **Supplementary Table 4: Genes enriched in contractile cell types and invertebrate**

1063 **stem cells highlighted in Figure 4D.** The IDs of the genes enriched in the contractile

1064 and invertebrate stem cell types are provided along with the IDs of the EggNOG orthology

1065 groups to which they belong. In cases where multiple genes from a species belonging to

1066 the same orthology group are enriched, the most differentially expressed gene is shown.

1067 The descriptions in the stem cell table are orthology annotations associated with the

1068 *Spongilla* genes provided in the original study (Musser et al., 2019).

1069

1070 **Supplementary Table 5: Cell types in the cell type families shown in Figure 4D.** For

1071 the schistosome cell types, we annotated two neural clusters, both of which express the

1072 neural marker *complexin* (Li et al., 2020). One of the clusters expresses the antigen

1073 *SmKK7*, so we label the clusters “Neural” and “Neural\_KK7”, respectively. The “Muscle”

1074 population contains non-neoblast cells expressing *troponin*. The “Tegument\_prog” and

1075 “Tegument” populations consist of cells expressing tegument progenitor and

1076 differentiated marker genes, respectively, as reported in a previous study (Wendt et al.,

1077 2018).